Spreading of the Indonesian Throughflow in the Indian Ocean*

QIAN SONG, ARNOLD L. GORDON, AND MARTIN VISBECK

Department of Earth and Environmental Sciences, Lamont-Doherty Earth Observatory, Columbia University, Palisades, New York

(Manuscript received 27 March 2003, in final form 19 August 2003)

ABSTRACT

The Indonesian Throughflow (ITF) spreading pathways and time scales in the Indian Ocean are investigated using both observational data and two numerical tracer experiments, one being a three-dimensional Lagrangian trajectory experiment and the other a transit-time probability density function (PDF) tracer experiment, in an ocean general circulation model. The model climatology is in agreement with observations and other model results except that speeds of boundary currents are lower. Upon reaching the western boundary within the South Equatorial Current (SEC), the trajectories of the ITF tracers within the thermocline exhibit bifurcation. The Lagrangian trajectory experiment shows that at the western boundary about 38%±5% thermocline ITF water flows southward to join the Agulhas Current, consequently exiting the Indian Ocean, and the rest, about 62%±5%, flows northward to the north of SEC. In boreal summer, ITF water penetrates into the Northern Hemisphere within the Somali Current. The primary spreading pathway of the thermocline ITF water north of SEC is upwelling to the surface layer with subsequent advection southward within the surface Ekman layer toward the southern Indian Ocean subtropics. There it is subducted and advected northward in the upper thermocline to rejoin the SEC. Both the observations and the trajectory experiment suggest that the upwelling occurs mainly along the coast of Somalia during boreal summer and in the open ocean within a cyclonic gyre in the Tropics south of the equator throughout the year. All the ITF water eventually exits the Indian Ocean along the western boundary within the Mozambique Channel and the east coast of Madagascar and, farther south, the Agulhas Current region. The advective spreading time scales, represented by the elapsed time corresponding to the maximum of transit-time PDF, show that in the upper thermocline the ITF crosses the Indian Ocean, from the Makassar Strait to the east coast of the African continent, on a time scale of about 10 yr and reaches the Arabian Sea on a time scale of over 20 yr.

1. Introduction

The low-salinity Indonesian Throughflow (ITF) thermocline water entering the Indian Ocean by way of the Timor Sea is slowly diluted as it is advected westward within the South Equatorial Current (SEC) between 10° and 20°S (Gordon 1986). The ITF component of the SEC 30–40-Sv (Sv $\equiv 10^6$ m^3 s^{-1}) total transport (Fine 1985; Schott and McCreary 2001) varies from 4 to 12 Sv (Gordon et al. 1997; Garternicht and Schott 1997; Potemra et al. 1997; Schott and McCreary 2001), the variation presumably a result of changes in the ITF injection rate and variations in definitions and methods of analysis. The mean and variable characteristics of the ITF strongly influence the heat and freshwater budgets of the Indian Ocean (Godfrey 1996; Lukas et al. 1996; Webster et al. 1998; Murtugudde et al. 1998; Schiller et al. 1998; Murtugudde and Busalacchi 1999; Garternicht and Schott 1997; Hirst and Godfrey 1993; Lee et al. 2002; Schneider 1998; Verschell et al. 1995; Wajsowicz 2001; Wajsowicz and Schneider 2001). To close the mass balance, all ITF water must eventually exit the Indian Ocean, in all probability within the Agulhas Current (Vranes et al. 2002). The model results of Haines et al. (1999) show that 87% of the ITF water exits the Indian Ocean through the Agulhas Current region 50 years after it enters the Indian Ocean. The pathways followed by the ITF water enroute to the Agulhas Current are a decisive factor determining how the ITF affects the stratification and air–sea heat fluxes in the Indian Ocean.

The pathways leading ITF water to the Agulhas Current within the Indian Ocean are ambiguous. The western Indian Ocean general circulation pattern is discussed by Quadfasel (1982), Tomczak and Godfrey (1994), and Schott and McCreary (2001). Along the east coast of Madagascar, one branch of the SEC, the Southeast Madagascar Current (SEMC) flows southward carrying 20.6±6 Sv water (Swallow et al. 1988). The other branch, the Northeast Madagascar Current (NEMC), finds its way northward past the northern tip of Madagascar contributing to the East African Coast Current

* Lamont-Doherty Earth Observatory Contribution Number 6568.

Corresponding author address: Qian Song, 202A Oceanography, Lamont-Doherty Earth Observatory, 61 Route 9W, Palisades, NY 10964.
E-mail: qsong@ldeo.columbia.edu

(EACC), which evolves into the northward flowing Somali Current in boreal summer and merges with the southward flowing Somali Current in boreal winter to enter the South Equatorial Countercurrent (SECC). Because of an active eddy field in the Mozambique Channel [Donguy and Piton 1991; Gründlingh 1985, 1993; de Ruijter et al. 2002; and in the Los Alamos National Laboratory 0.1°-resolution model (M. Maltrud 2001, personal communication)] and sparse data, the geostrophic transport through the Mozambique Channel is not well resolved. Estimates vary from 5 Sv northward to 29 Sv southward (Sætre and de Silva 1984; Fu 1986; Harris 1972; Macdonald and Wunsch 1996; Macdonald 1998; Ganachaud et al. 2000; DiMarco et al. 2002).

Several studies have been done on the spreading pathways and time scales of the ITF in the Indian Ocean but none of them provide a complete three-dimensional picture of the ITF water spreading. Using hydrographic data and a mixing model that combines cluster analysis with optimum multiparameter analysis, You and Tomczak (1993) and You (1997) study the spreading of ITF water, among other water masses, in the thermocline of the Indian Ocean. In a trajectory experiment in a thermocline layer of a four-layer ocean circulation model, Haines et al. (1999) investigate the ITF spreading pathways and time scales only in the thermocline. The vertical transfer of the ITF water between the thermocline and the surface layer, which is crucial in the process of air–sea interaction, is consequently excluded from their study.

The intent of this paper is to study the ITF spreading pathways and time scales in the Indian Ocean from both comprehensive hydrographic data and tracer experiments in an ocean general circulation model (OGCM). We first trace the ITF water by its temperature and salinity characteristics using hydrographic data. However, the ITF water is highly modified by mixing and sea–air fluxes within the Indian Ocean, and so one cannot in traditional watermass sense follow the ITF water beyond its presence as an isohaline layer in the tropical thermocline. So what we attempt to do in a three-dimensional Lagrangian trajectory experiment is to tag the ITF water in the Indonesian seas and trace its dispersal within the Indian Ocean. Strictly speaking, the term ''ITF water'' is attached to a water mass with certain temperature and salinity characteristics. For simplicity in the trajectory experiment we use ''ITF water'' to refer to the ITF water that we tag in the Indonesian seas so that we can still use this term after the ITF water—in traditional watermass sense—is transformed and loses its temperature and salinity properties. To estimate the ITF spreading time scales in the thermocline a probability density function (PDF) of ITF-to-$\mathbf{X}$ ($\mathbf{X}$ represents points in the Indian Ocean) transit times is employed and a tracer that can technically generate the PDF is applied in the OGCM. The concept of transit-time PDF is first introduced to investigate the flow of tracers in natural reservoirs and, in particular, groundwater (Bolin and Rodhe 1973; Nir and Lewis 1975). Recently, it is employed in studies of tracers in the stratosphere (Kida 1983; Hall and Plumb 1994; Holzer and Hall 2000) and ventilation processes in the ocean (Beining and Roether 1996; Khatiwala et al. 2001). In essence, the transit-time PDF (or age spectrum in some other literature) is a characteristic of the flow, independent of the distribution of any tracer, and summarizes the rate at which fluid is transported from a source region Ω to a point $\mathbf{X}$ (Holzer and Hall 2000). The transit-time PDF describes more accurately the ITF water spreading time scales than do other techniques.

Note that seasons are referenced to the Northern Hemisphere throughout the paper. The paper is organized as follows: The dataset and the OGCM are described in section 2. Results from observations are presented in section 3. Section 4 assesses the model performance. The Lagrangian trajectory experiment is discussed in section 5, and the transit-time PDF tracer experiment in section 6, followed by a discussion in section 7 and summary in section 8.

2. Description of observational data and model

The dataset used in this paper consists of World Ocean Circulation Experiment (WOCE), the Reid–Mantyla dataset, and National Oceanographic Data Center (NODC) data. The high-resolution WOCE hydrographic program (WHP) sections in the Indian Ocean were collected in 1995 and 1996. The Reid–Mantyla dataset consists of stations obtained mainly from the 1960s to 1980s. Although its quality and resolution are not as high as the WHP section data, the Reid–Mantyla data have reasonable accuracy for the purpose of this paper. While NODC data are comprehensive in terms of the diversity of the data sources, some measurements were taken as early as 1910s, and there are errors in the data archive due to its various sources and calibration standards. Suspicious data were eliminated from the dataset.

The OGCM used in this study is the Lamont Ocean–Atmosphere Mixed Layer (AML) Model. It is a primitive equation OGCM derived from the Gent and Cane (1989) model. The model bathymetry is the averaged U.S. Navy's ETOPO5 5-min bathymetry. The model domain covers 50°S–30°N, 0°–150°E (Fig. 1). Only the Makassar Strait is left open as a passage for the ITF. Other channels within the Indonesian seas are artificially closed. To save computer time, part of Australia is cut off. Because the focus of this study is the ITF, which is mainly in the thermocline, fine vertical resolution is used in the upper 400 m. There are 28 layers in the model with 19 of them in the upper 400 m. The layers are centered at 5, 15, 25, 35, 45, 55, 65, 75, 85, 95, 110, 130, 150, 170, 190, 210, 250, 300, 390, 490, 600, 800, 1000, 1200, 1500, 2000, 3000, and 4000 m. Horizontal grid stretching is used in regions of interest, that is, latitudinal stretching in the tropical region (5°N–15°S) and the longitudinal stretching in the Somali Cur-

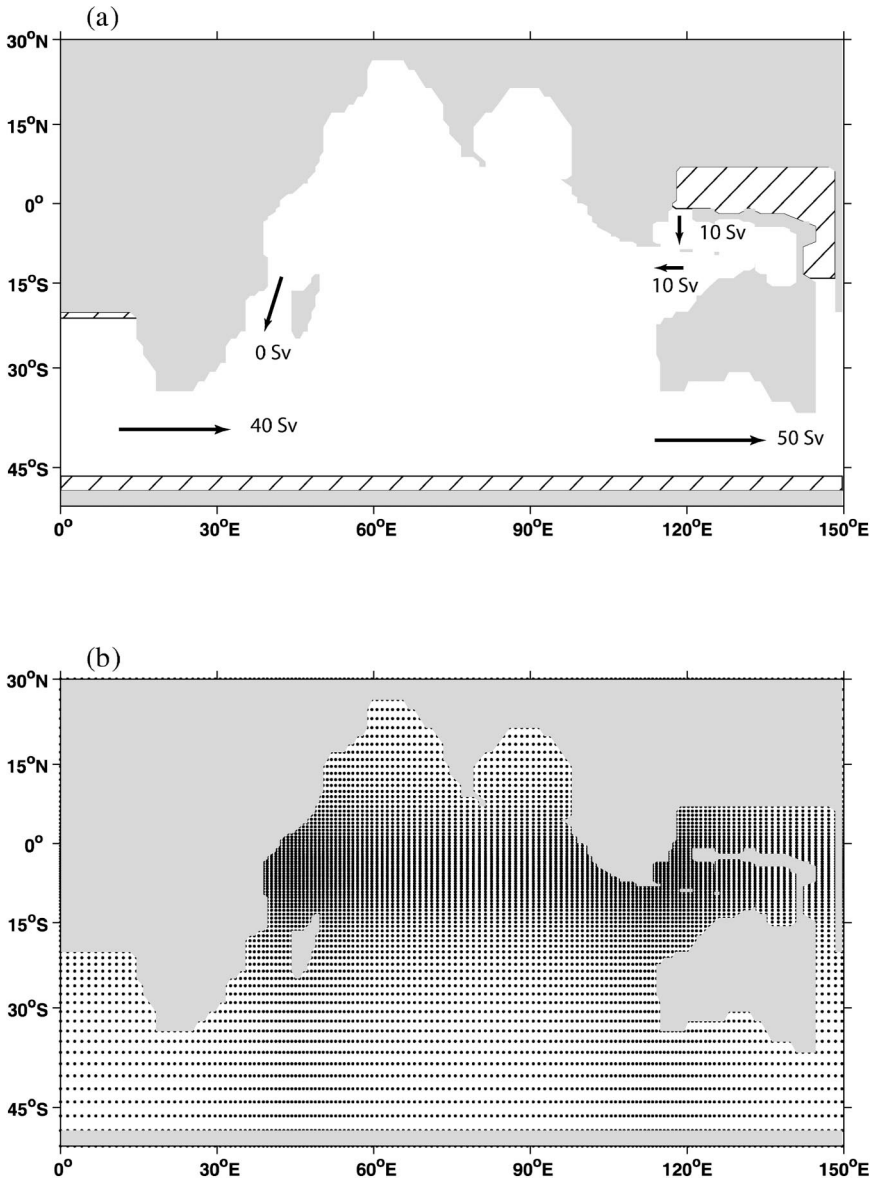

FIG. 1. (a) Model domain: the hatched areas indicate model sponges. The arrows and numbers indicate the direction and magnitude of the prescribed depth-integrated transport of ITF, the flow through the Mozambique Channel, and the Antarctic Circumpolar Current. (b) Model horizontal grid.

rent region, the Mozambique Channel, and the Leeuwin Current region (Fig. 1b). The zonal resolution is 0.5° in the Tropics and decreasing gradually to 1.7° in extratropics. The meridional resolution is about 0.8° in the Somali Current region, the Mozambique Channel, and in the Leeuwin Current region and falls off to 1.2° for the most of the ocean.

The model is forced by global monthly ocean wind stress climatology based on European Centre for Medium-Range Weather Forecasts (ECMWF) analyses (Trenberth et al. 1989). The sea surface temperature and sea surface salinity are restored to Levitus monthly climatology (Levitus 1994) with a restoring time scale of 1 month. Sponges are applied in the region north of the Makassar Strait and at the southern boundaries (Fig. 1a). Temperature and salinity in the sponge layers are restored to Levitus seasonal climatology (Levitus 1994) with a restoring time scale of 6 months. At the east and west boundaries of the Antarctic Circumpolar Current (ACC) periodic boundary conditions are used. The wind stress and hydrographic data sets are interpolated onto the model grid using linear interpolation in x and y direction separately.

Lateral mixing of temperature, salinity, and tracers is

accomplished by a modified Griffies (1998) implementation of the eddy parameterization scheme of Gent and McWilliams (1990). The coefficient for both the isopycnal diffusion and the eddy-induced transport is set to be 400 $m^2\ s^{-1}$. A fourth-order Shapiro filter is used on the momentum equations with reduced order approaching boundaries.

For vertical mixing, convective adjustment and the Richardson-number-dependent mixing of Pacanowski and Philander (1981) are used. In addition, a uniform background vertical diffusivity of $10^{-4}\ m^2\ s^{-1}$ for momentum and $10^{-5}\ m^2\ s^{-1}$ for temperature, salt, and tracers is used everywhere.

The model has a rigid lid at the surface, so one way that is implemented in the model to have transports around islands is to explicitly specify the magnitudes of the depth-integrated transports around them, which is equivalent to specify the values of barotropic streamfunctions of various islands in the model domain. In this study the values of barotropic streamfunctions of the Asia–Africa continent, Australia, Madagascar, and the southern boundary are set to be 0, −10, 0, and 40 Sv, respectively, so that the depth-integrated transports of the ITF (between the Asia–Africa continent and Australia), the flow through the Mozambique Channel (between the Asia–Africa continent and Madagascar), and the ACC (between the Asia–Africa continent and the southern boundary) are 10, 0, and 40 Sv, respectively. ITF transport estimates vary from 0 to 30 Sv (see the reviews of Godfrey 1996; Schott and McCreary 2001). However, 10 Sv is generally considered a reasonable value as the climatological mean of ITF transport (Gordon 2001). Previous estimates of the transport through the Mozambique Channel based on hydrographic data range from 5 Sv northward to 26 Sv southward (DiMarco et al. 2002). Direct LADCP observations of WOCE WHP lines 12 and 14 are found difficult to use for transport estimates because of the large error bars associated with them (DiMarco et al. 2002). So there is no reliable observational estimate of the total transport through the channel to help us specify the corresponding value in the model. We have performed a set of sensitivity experiments with various transport magnitudes through the channel and found that 0 Sv transport gives the most reasonable circulation around Madagascar—mainly the NEMC and SEMC. Moreover, note that 0 Sv depth-integrated transport through the channel does not mean that there is no flow through the channel at all; for example, the transport in the upper 500 m is 4.6 Sv southward at 20°S. The transport of the ACC (40 Sv) in the model is smaller than the total transport of the current (over 100 Sv) because the model southern boundary is not far south enough to accommodate the whole ACC. Furthermore, the sponge layer at the southern boundary keeps the model temperature and salinity structure close to observations. Hence, the effects of the weaker ACC on the tropical circulation can be neglected, which is further justified by a sensitivity experiment with ACC transport of 60 Sv. The model is spun up for 50 years, which is long enough for the upper 500 m to reach steady state, followed by another 31-yr run in the transit-time PDF tracer experiment.

3. Observations

Data used in this section are the combination of the three data sources described in section 2.

a. Salinity distribution on the $\sigma_0 = 25.0$ surface

We map the salinity distribution on the $\sigma_0 = 25.0$ surface for each monsoon season (Figs. 2a and 3a) to trace the spreading of the low salinity ITF water. The salinity on the $\sigma_0 = 25.0$ surface was calculated by a second-order interpolation of the data above and below the surface. Should there be no data within $\sigma_0 = 25.0 \pm 0.2$, the station is eliminated. Horizontally, the data are smoothed by using a Gaussian filter with a width of 10°. Following the time honored method of descriptive oceanography, that spreading is marked by a ''tongue'' configuration in the isohalines, with the direction of spreading along the tongue axis, we find in both seasons westward spreading of the low salinity ITF water centered at 10°S. In winter the axis of the low salinity feature is slightly farther south than that in summer.

North of 10°S, significant seasonal variation is observed. In summer, low-salinity water is traced spreading northward within the Somali Current. In winter, the spreading of the low-salinity water is confined at low latitudes, a consequence of the Somali Current reversal. High salinity is attained in the Arabian Sea thermocline in both seasons. In summer an arm of saline Arabian Sea Water (ASW) is projected toward the southeast near 70°E to extend eastward along the equator. This is the ''Southwest Monsoon Current'' (SMC). Lower-salinity thermocline water is observed just south of India near 5°N. The same pattern, though weaker, is observed in winter.

The strongest presence of ITF thermocline water in the Mozambique Channel occurs in the western part, whereas in the eastern part of the channel higher-salinity thermocline water is drawn from the SEMC curling around the southern tip of Madagascar into the Mozambique Channel.

b. Watermass analyses

Four water masses compose the thermocline of the Indian Ocean [see Wyrtki (1971), Warren et al. (1966), Warren (1981), Tomczak and Godfrey (1994), and Schott and McCreary (2001) for more detailed description of water masses]. The ASW, formed in the northern Arabian Sea, and the Subtropical Subsurface Water (SSW), formed in the Southern Hemisphere subtropical convergence zone, spread as salinity maxima at core densities of $\sigma_0 = 25.0$ and 25.8, respectively. The South

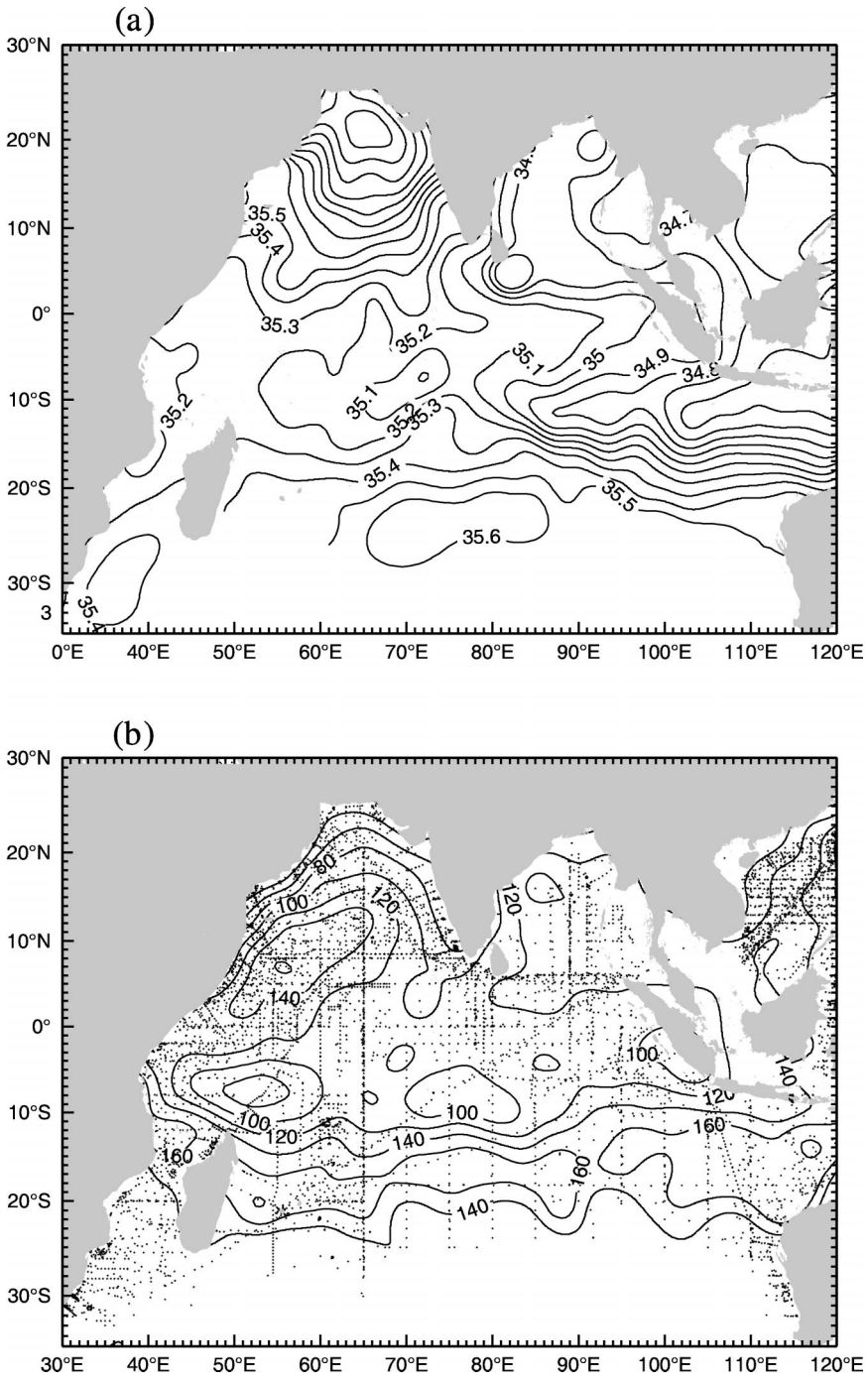

FIG. 2. (a) Salinity distribution on the potential density surface of $\sigma_0 = 25.0$ in northern summer (Jul–Sep). The increment of the contours is 0.1. (b) The pressure (dbar) on the surface $\sigma_0 = 25.0$. Dots represent stations used in the calculations.

Indian Central Water (SICW) is formed by subduction in the southern subtropics and is characterized by a near-linear temperature/salinity (T/S) relation between the salinity maximum of SSW and minimum of Antarctic Intermediate Water. The nearly isohaline ITF water is derived from Pacific Ocean central water and modified in the Indonesian Seas. Since the northern Indian Ocean does not have a subtropical convergence zone, it is suggested that the northern Indian thermocline may be ventilated from the south by SICW and ITF water (Warren

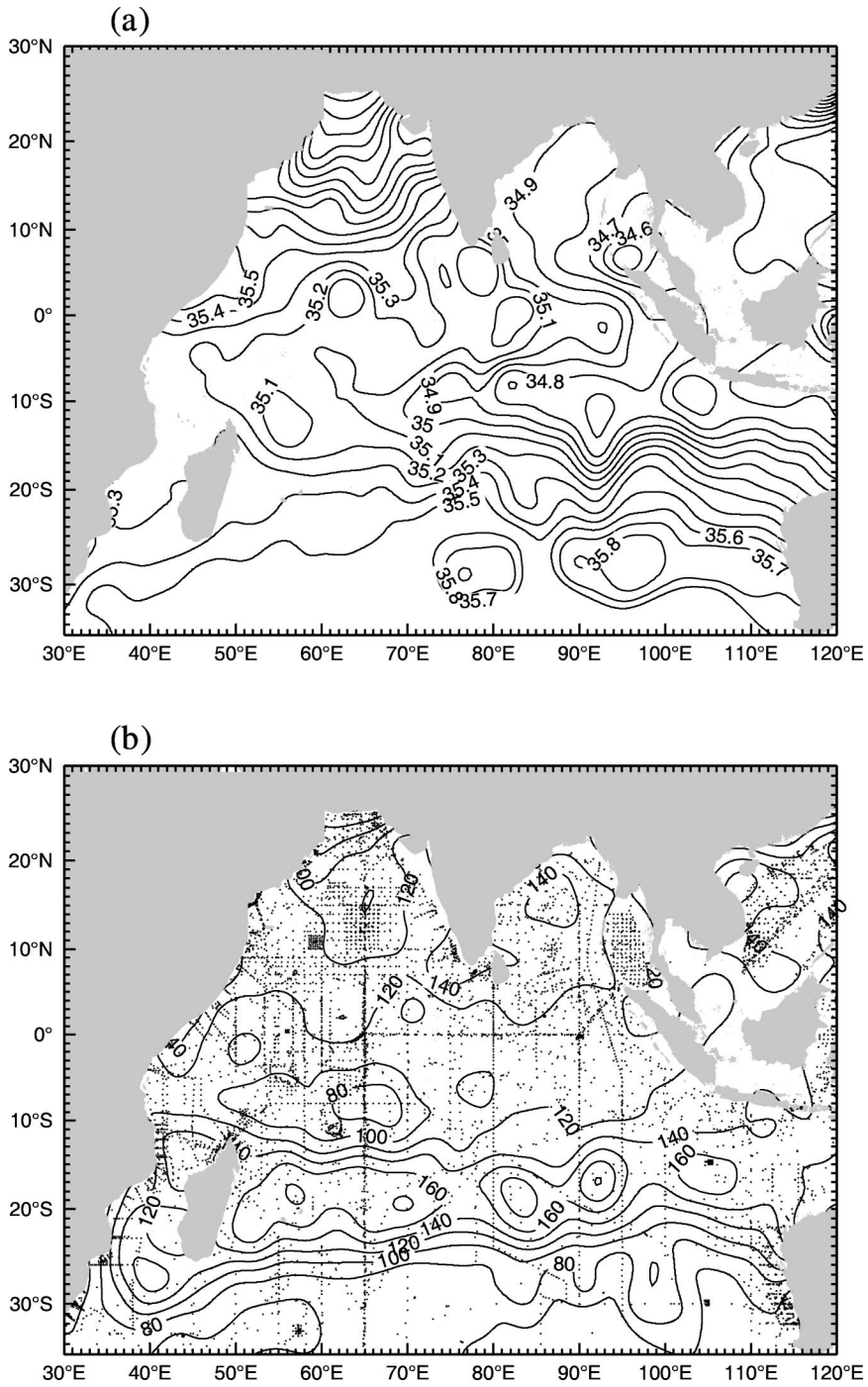

FIG. 3. As in Fig. 2 but for northern winter (Jan–Mar).

et al. 1966; Swallow 1984; Olson et al. 1993; You and Tomczak 1993).

The potential temperature–salinity (θ–S) relation for the summer and winter (Fig. 4) is presented for three sections: the ''SEC'' section, along 65°E from 8° to 18°S, to define the inflow within the SEC; the ''Somali'' section, 5°N from 45° to 62°E, to resolve the northward spreading of ITF water within and east of the Somali Current; and the ''Mozambique and Madagascar'' section, 20°S from 35° to 53°E, to resolve the ITF water within Mozambique Channel and east of Madagascar.

In both seasons at the 65°E SEC section, the θ–S relation between $\sigma_0 = 24.0$ and 26.0 displays the relatively isohaline characteristics depicting the defining property imposed by the ITF water (Gordon et al. 1997). Mixing of the ITF water with the more saline water of

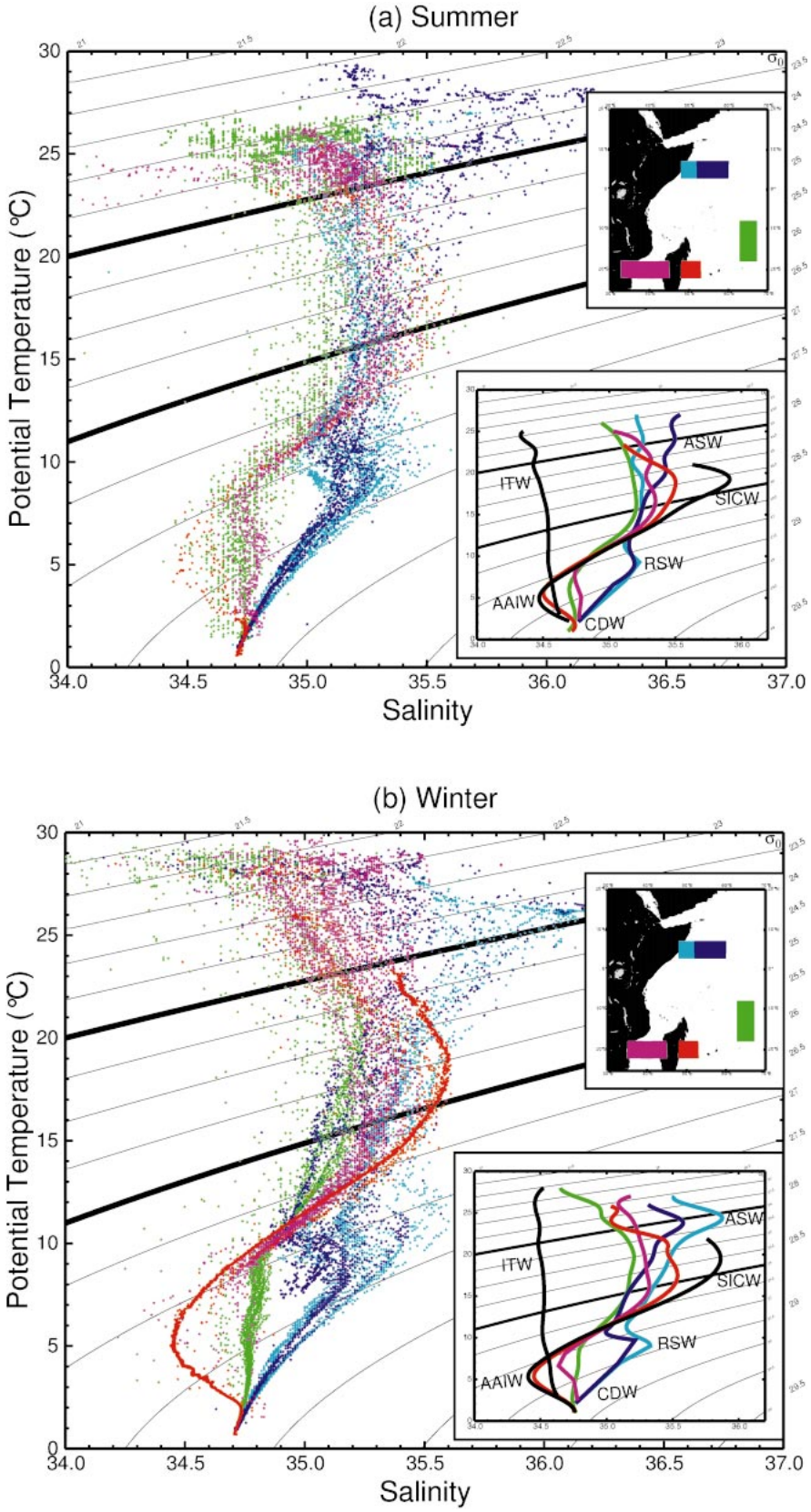
(a) Summer
Potential Temperature (°C)
Salinity
ITW
ASW
SICW
RSW
AAIW
CDW
(b) Winter
Potential Temperature (°C)
Salinity
ITW
ASW
SICW
RSW
AAIW
CDW

the Indian Ocean leads to significantly higher salinity in the stratum ($S = 35.2$) than the typical salinity ($S = 34.4$–34.6) of the ITF water introduced into the Indian Ocean from the Timor Sea. Comparing the depth of $\sigma_0 = 24.0$ surface with the deepest mixed layer depth (Rao et al. 1989; Kara et al. 2002), we find that the local mixed layer and associated localized air–sea fluxes do not reach into the $\sigma_0 = 24.0$ and 26.0 layer of the tropical Indian Ocean (20°S–10°N).

At the 5°N ''Somali'' section, conspicuous differences in θ–S characteristics are observed in different seasons. In summer (Fig. 4a), the θ–S properties of the near-coast water (52°–60°E) across 5°N are almost the same as those of the water flowing within the SEC at 65°E, which is consistent with previous results that show that during the southwest monsoon the north branch of the SEC feeds into the EACC and then supplies the northward flowing Somali Current [see Schott and McCreary (2001) for an excellent review on the circulation in the Indian Ocean]. In winter (Fig. 4b), the salinity at the same section increases significantly and the θ–S properties are more like those of the ASW, which is also consistent with the direction of the Somali Current during the northeast monsoon.

At the 65°E SEC and 20°S Mozambique and Madagascar sections, there is only weak seasonal variability. In the Mozambique Channel (20°S, 35°–45°E), the low salinity ($S = 35.3$) with little vertical variation between $\sigma_0 = 24.0$ and 26.0 implies the presence of ITF water. Recent CTD data (de Ruijter et al. 2002) show that the θ–S characteristics of the thermocline water in the Mozambique Channel are much like those of the SEC. Along the east coast of Madagascar (20°S, 48°–53°E), the dominant salinity maximum is of SICW origin, though presence of ITF water is divulged by the slightly lower salinity of the salinity maximum relative to the typical value of SICW farther to the east. The salinity maximum of 35.6 is much higher than the salinity within the SEC ($S = 35.0$–35.2), suggesting the percentage of ITF water along the east coast of Madagascar is lower than that within the Mozambique Channel. However, we are not able to draw any conclusion on whether the Mozambique Channel or the east coast of Madagascar delivers more ITF water southward because that depends on not only the presence of ITF thermocline water but also transport, which is not resolved by the property distribution.

In summary, the θ–S characteristics reveal the distribution of ITF water within the thermocline of the western Indian Ocean. Upon reaching the western boundary within the SEC, ITF water spreads southward into the Mozambique Channel and along the east coast of Madagascar in both seasons and northward in the northern summer within the Somali Current north of 10°S.

c. Upwelling and Ekman transport

An important question to answer is how does the ITF water in the thermocline that is advected north of the SEC eventually exit the Indian Ocean through the southern boundary? It is beyond the ability of hydrographic data to unambiguously answer the question because the ITF water loses its defining *T*/*S* properties beyond the southern tropical Indian Ocean thermocline. Our hypothesis is that the ITF water is transferred into the surface layer by Ekman-induced upwelling and then transported southward by Ekman transport during the summer monsoon. Upwelling of the thermocline water is documented off the coast of Somalia, Oman, and India in the northern summer and in the open ocean within the cyclonic gyre, with the SEC and SECC as the southern and northern boundaries between 5° and 10°S and between 50° and 90°E (Schott et al. 2002). The cyclonic gyre is referred to as ''South Equatorial Gyre'' (SEG) in this paper. The coastal upwelling occurs in the summer season and the annual mean magnitude is estimated as about 5 Sv by Schott et al. (2002). The existence of open-ocean upwelling related to the SEG is supported by satellite imagery of ocean color, which sometimes shows the presence of phytoplankton blooms in this region (Murtugudde et al. 1999). It is also implied by the year-round Ekman divergence in this region, which Schott et al. (2002) estimate an annual mean magnitude of about 10 Sv in the box 2°–12°S and 50°–90°E based on National Centers for Environmental Prediction (NCEP) and *European Remote Sensing Satellite* (*ERS*)-*1/2* scatterometer wind stresses. In addition, we compute the Ekman divergence in the region 2.5°–12.5°S, 50°–90°E from the monthly wind stress climatology based on ECMWF analysis (Trenberth et al. 1989) as 1.9 Sv in winter, 14.3 Sv in spring, 8.7 Sv in summer, and 16.2 Sv in autumn with an annual mean of 10.3 Sv.

The meridional Ekman transport in the Indian Ocean on both sides of the equator is southward from April through October (Levitus 1988; Schott and McCreary

←

FIG. 4. The potential temperature–salinity (θ–S) characteristics in northern (a) summer (Jul–Sep) and (b) winter (Jan–Mar) of waters from several sections. The sections are 65°E from 8° to 18°S (green), 5°N from 45° to 52°E (light blue), 5°N from 52° to 62°E (dark blue), 20°S from 35° to 45°E (pink), and 20°S from 48° to 53°E (red). Sections correspond to SEC, Somali Current, east of the Somali Current, Mozambique Channel, and the east coast of Madagascar, respectively. Curves are fitted for each section and are shown in the lower-right insert. The θ–S curves of the Indonesian Throughflow water (ITW) in the Timor Sea (CTD data from *Arlindo* 1993/94 cruises) and the South Indian Central Water (SICW) (data from stations in the box of 25°–30°S, 70°–80°E) are shown as black lines in the insert. The water masses indicated are Arabian Sea Water (ASW), Red Sea Water (RSW), Antarctic Intermediate Water (AAIW), and Circumpolar Deep Water (CDW). The $\sigma_0 = 24.0$ and $\sigma_0 = 26.0$ isopleths are darkened.

2001; Schott et al. 2002). The magnitude of the Ekman transport peaks during the summer monsoon (June–September) with zonally integrated value as large as 30–40 Sv within 10°S–10°N (Levitus 1988). The southward Ekman transport on both sides of the equator is connected by the shallow meridional overturning circulation, referred to as the equatorial roll by Schott et al. (2002), within a narrow band around the equator.

The observations show the capability of the upwelling and Ekman transport in transporting ITF water out of the northern Indian Ocean toward the southern boundary. To further justify this hypothetical pathway we turn to a three-dimensional Lagrangian trajectory experiment (section 5).

4. Model climatology

Model climatology is calculated by taking the average of the last 10 years of the spinup stage. The average model horizontal circulation in the upper 150 m is shown in Fig. 5 for the two typical monsoon months: February (northeast monsoon) and August (southwest monsoon). The model well reproduces all major currents of the Indian Ocean. The seasonal reversal of the Somali Current is clearly shown in the two monsoon months with peak speeds about 2 m s^{-1} in August, which is greater than the average speeds from ship drift and drifter data (Culter and Swallow 1984; Richardson and McKee 1989; Quadfasel and Cresswell 1992; Molinari et al. 1990; Shenoi et al. 1999) but weaker than synoptic cruise measurements (Swallow et al. 1983), as in models of McCreary et al. (1993) and Murtugudde and Busalacchi (1999). The structure of the Somali Current is also reasonably reproduced, including the ''Southern Gyre'' (3°–4°N) and the Great Whirl (9°N) in August and the northward undercurrent at equator in winter. The anticyclonic circulation in August over the Arabian Sea and the anticyclonic gyre over the Bay of Bengal in February are consistent with ship drift climatology and other models (e.g., McCreary et al. 1993; Murtugudde and Busalacchi 1999). The monsoon currents between Sri Lanka and the equator, SMC in August and Northeast Monsoon Current (NMC) in February, are well resolved with speeds of about 0.5 m s^{-1} at surface in both seasons that are comparable with ship drift and drifter data but smaller than mooring observations (~0.9 m s^{-1}; Schott et al. 1994). The model equatorial currents reverse direction four times per year: eastward equatorial jets (EJ; Wyrtki 1973) during the transition seasons (May and November) and westward flows during both monsoon seasons. The EJ in spring has speeds about 1 m s^{-1} at 80°E, whereas that in autumn is weaker with speeds about 0.7 m s^{-1}. The weaker EJ in autumn is somewhat at odds with ship drift data (Han et al. 1999), which show that both EJs have similar strength. However, similar results are observed in other models (McCreary et al. 1993; Murtugudde and Busalacchi 1999) and wind stress products maybe responsible for this shortcoming (Murtugudde and Busalacchi 1999). The model eastern boundary currents west of Sumatra is southeastward from April to December, while it turns to the northwest during January–March. That is also observed in other model simulations (e.g., McCreary et al. 1993), but the analyses of trajectories of drifting buoys (Quadfasel and Cresswell 1992; Molinari et al. 1990; Shenoi et al. 1999) show year-round southward flow. The reason for the discrepancy between the modeled and observed flow is not clear. The SECC, formed by the confluence of the EACC and the southward Somali Current in winter, flows between 4° and 8°S with peak speeds of 0.5 m s^{-1} in the west, which is also in agreement with ship drift data.

The speeds of SEC at surface (~0.5 m s^{-1}) are slightly higher than ship drift data. The bifurcation of SEC at the east coast of Madagascar into NEMC, flowing around the northern tip of Madagascar, and the SEMC, flowing along the east coast of Madagascar, is clearly shown. The NEMC feeds into the southward Mozambique Channel Current and the northward EACC. The maximum annual-mean speed of the NEMC is about 0.5 m s^{-1}, slightly lower than 0.6 m s^{-1} from mooring observations, whereas that of SEMC has speeds about 0.3 m s^{-1}, significantly weaker than 0.7 m s^{-1} from mooring observations of Schott et al. (1988). Because of insufficient model resolution in the Mozambique Channel, the barotropic eddies (de Ruijter et al. 2002) are not recovered in the model. South of Madagascar the Mozambique ''retroflection'' is not reproduced in the model, and farther south the Agulhas rings are not resolved as a result of coarse model resolution in the southern Indian Ocean.

Along the west coast of Australia the Leeuwin Current in the model flows poleward most of the year. However, a couple of features of the Leeuwin Current in the model do not agree with observations (Smith et al. 1991; Holloway 1995) very well. The annual mean poleward transport of the Leeuwin Current in the model is about 1 Sv, much smaller than 4 Sv estimated from current-meter observations (Smith et al. 1991). That is probably due to the coarse grid spacing in the Leeuwin Current region in the model, which is about 0.8° in longitude and much larger than the internal radius of deformation. In addition, most of the water within the Leeuwin Current in the model is from the Tropics, which renders the salinity off the west coast of Australia in the model (Fig. 7) lower than observations (Figs. 2 and 3, Ridgway et al. 2002).

Meridional sections of potential temperature, salinity, and geostrophic velocity for summer (July–September average) and winter (January–March average) along 65°E (Fig. 6) are presented accompanied by the corresponding sections from the Levitus seasonal climatology (Levitus 1994). The thermal structure is reasonably reproduced in the model, including the ther-

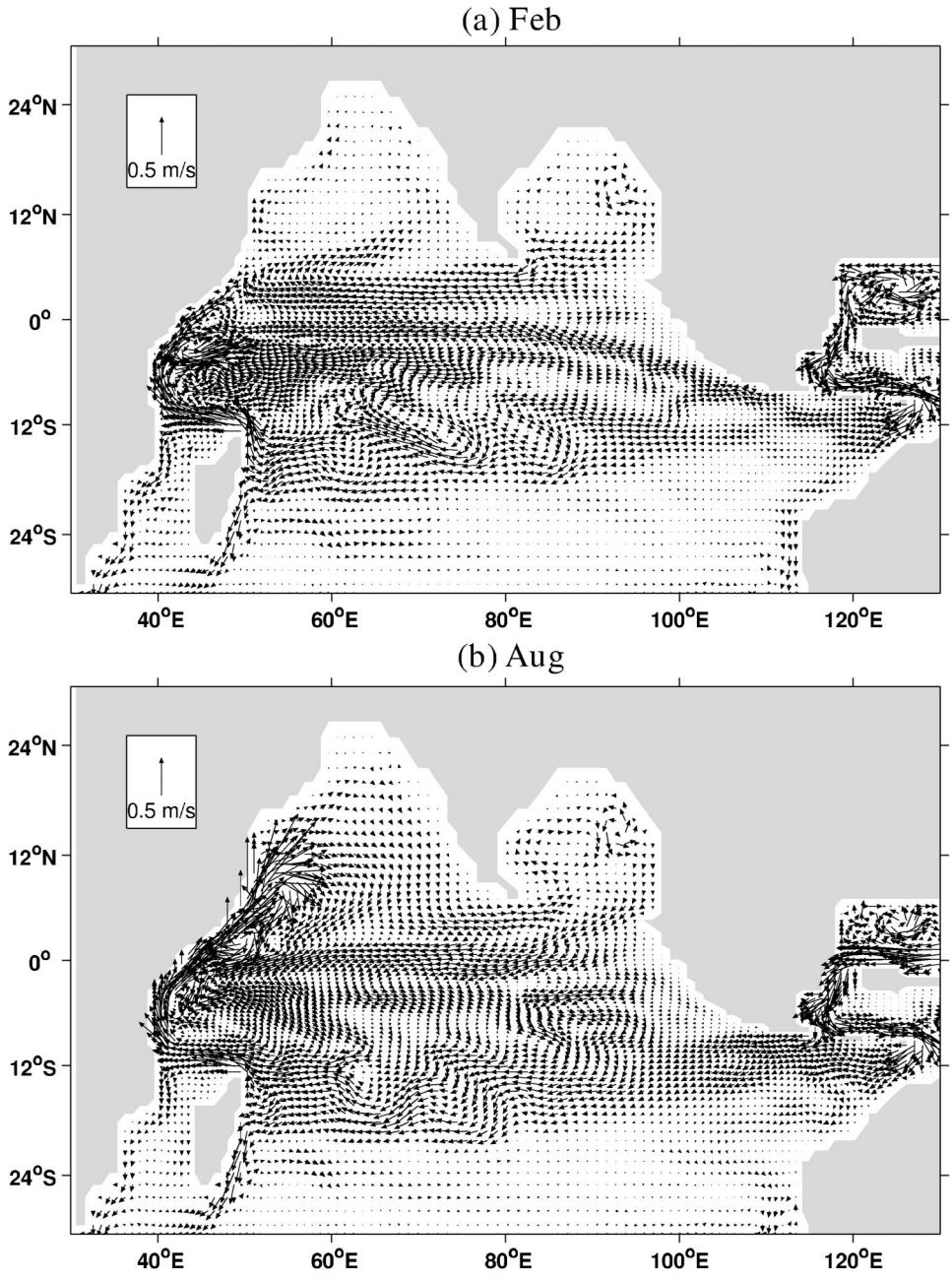

FIG. 5. Model climatological currents averaged in the upper 150 m in (a) Feb (northeast monsoon) and (b) Aug (southwest monsoon).

mocline uplift around 10°S that is, especially in summer, about 2°–3° south of that in the Levitus climatology. The ITF water, shown as the isohaline patch around 10°S between 100 and 200 m, has a slightly larger meridional extent in the model than in the Levitus data. The geostrophic velocity of SEC is slightly stronger in the model, which may not be significant given that the Levitus data are smoothed in both time and space. The core of the SEC is narrower and centered south of that in Levitus climatology, particularly in summer, which is associated with the southward shift of the thermocline doom in the model relative to Levitus climatology.

The westward spreading of low-salinity ITF water is clearly shown on the isopycnal surface $\sigma_0 = 25.0$ (Fig. 7). The salinity is lower in the Arabian Sea because of the lack of high-salinity water input from the Red Sea and the Persian Gulf.

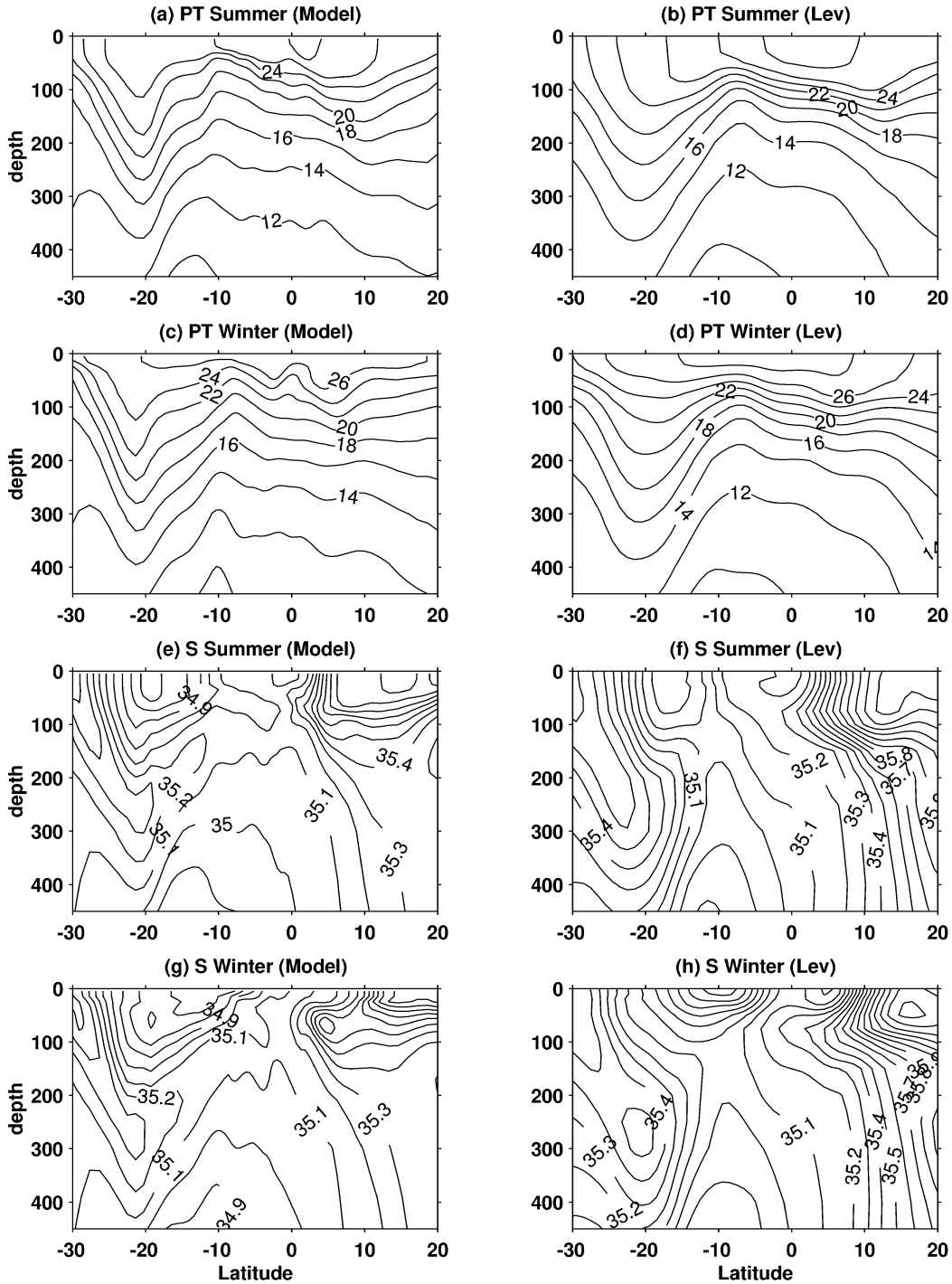

FIG. 6. (a), (c), (e), (g), (i), (k) Comparison of meridional sections of seasonal mean model potential temperature, salinity, and geostrophic velocity, and (b), (d), (f), (h), (j), (l) Levitus seasonal climatology along 65°E for both boreal summer and winter monsoon seasons.

In summary, the model surface currents in the interior of the basin are not significantly different from ship drift and drifter climatologies. Yet, because of the coarse model resolution, currents in the model are generally weaker than mooring and synoptic cruise observations, especially the boundary currents. That may affect our spreading time scale estimates, which will be further discussed in section 7a.

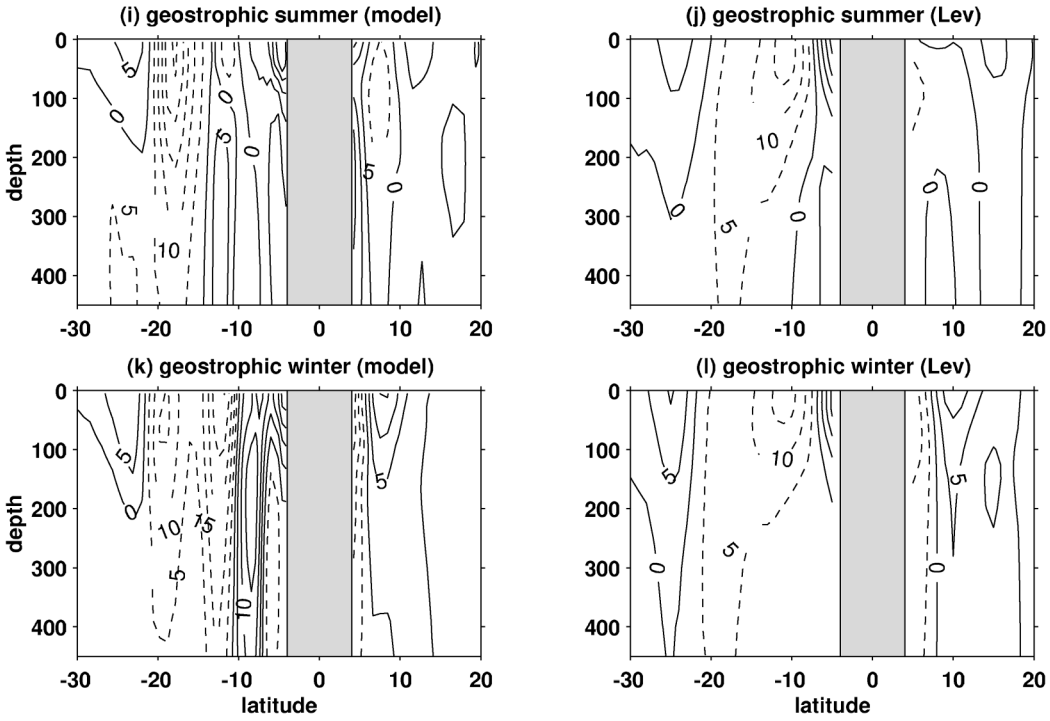

FIG. 6. (*Continued*)

5. Three-dimensional Lagrangian trajectory experiment

To further justify the hypothetical pathway followed by the ITF water north of SEC and construct a three-dimensional spreading pathway of the thermcline water originated from the Indonesian Seas in the Indian Ocean, an offline three-dimensional Lagrangian trajectory experiment is performed. The trajectory experiment has the advantage that it allows us to follow the water introduced from the Pacific to the Indian Ocean through the Indonesian seas even after it changes its *T*/*S* properties when hydrographic data are unable to trace the ITF water any more. The model monthly climatology, which is the average of the last 10 years of the spinup stage, is used in the experiment. The equation for particle trajectories is

$$\Delta\mathbf{X} = (\mathbf{U}_0 + \mathbf{U}^*)\Delta t + \boldsymbol{\zeta},$$

where $\mathbf{X}$ is the particle position, $\mathbf{U}_0$ is the large-scale model-resolved velocity, $\mathbf{U}^*$ is the eddy induced velocity in the Gent and McWilliams eddy parameterization scheme (Gent et al. 1995), and $\boldsymbol{\zeta}$ is the particle displacement due to turbulent diffusion. They are all vectors: Δt is the time increment, which is a day in this calculation; $\boldsymbol{\zeta}$ is parameterized as

$$\boldsymbol{\zeta} = \alpha(k\Delta t)^{-2}\mathbf{i} + \alpha(k\Delta t)^{-2}\mathbf{j} + \alpha(k\Delta t s^{-2})^{-2}\mathbf{k},$$

where α is a standard Gaussian random number, k (=400 $m^2\ s^{-1}$) is the model diffusion coefficient, and s is the isopycnal slope; $\mathbf{i}$, $\mathbf{j}$, and $\mathbf{k}$ are unit vectors of x, y, and z directions, respectively. Thus, the trajectories take into account not only large-scale model-resolved circulation, but also the eddy-induced transport and turbulent diffusion.

In each of the 12 experiments 100 particles are released in each month (January–December) in the thermocline (between σ_0 = 24.0 and 26.0) of the Makassar Strait, given that the ITF water is mainly advected into the Indian Ocean in the thermocline (Gordon et al. 1999; Fieux et al. 1996; Wijffels et al. 2002). Note that the term ''ITF water'' throughout this section is used to refer to the ITF water that we tag in the Makassar Strait rather than a water mass having specific temperature and salinity characteristics. Trajectories of 50 years are computed and the particle locations are saved every 10 days.

Even though all particles are initiated in the thermocline, with all of them between 100 and 250 m, their trajectories in the Indian Ocean are seen from the surface down to below 500 m. In addition, trajectories in different vertical layers have different geographic distribution (Fig. 8). The trajectories in the surface layer (<50 m) are mostly confined between 20°S and 8°N with farther northward intrusion along the western boundary, whereas those in the upper thermocline (50–200 m), basically following the wind-driven circulation, from a gyre in the southern equatorial region with some penetration into the Arabian Sea along the western boundary and southward stretching to the southern subtropical convergence zone where particles sink into

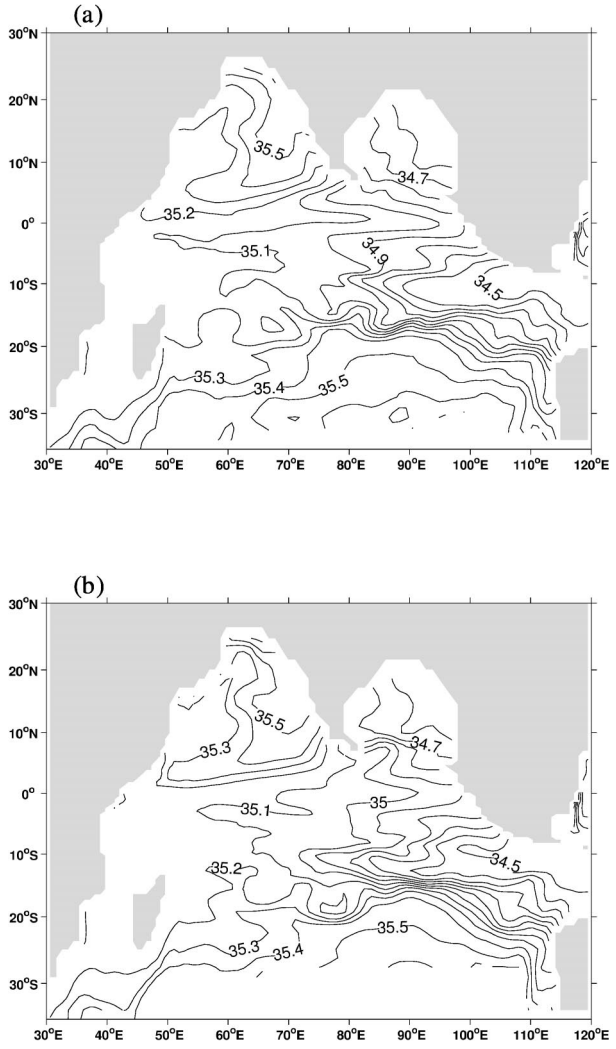

FIG. 7. Salinity distribution in the model on the potential density surface of $\sigma_0 = 25.0$ in (a) northern winter (Jan–Mar) and (b) northern summer (Jul–Sep).

deeper layers and recirculate in the subtropical gyre below 200 m in the southern subtropical gyre. The model fails to simulate the Madagascar retroflection south of Madagascar because of coarse model resolution; the trajectories there may not be accurate. For the same reason the model cannot resolve the Agulhas rings south of Africa. As a result almost all particles within the Agulhas Current return eastward within the ''Agulhas Returnflow,'' but in reality some of them must be transported to the Atlantic within these rings.

After 50 years 88%±2% (the mean and the standard deviation of the 12 experiments) particles escape the Indian Ocean across 34°S, which is consistent with Haines et al. (1999). All particles do so along the western boundary in the Agulhas Current region, as suggested by Vranes et al. (2002). A few particles advected to the south within the Leeuwin Current join the southern subtropical gyre off the west coast of Australian and then flow to the western boundary within the SEC.

Once the particles reach the western boundary within the SEC, 38%±5% particles flow to the south both through Mozambique Channel and along the east coast of Madagascar, while the rest (62%±5%) turn to the north within the EACC. Now the question is how the particles flowing to the north of the SEC turn to the southern boundary. In the following we test the idea proposed in section 3 that upwelling and Ekman transport may be important in exporting ITF water out of the region north of the SEC.

Most particles north of the SEC are indeed seen to be transferred from the thermocline into the surface layer through upwelling. Figure 9a shows that upwelling mainly occurs along the coast of Somalia in the equatorial region, especially the western part, and in the open ocean region between 60° and 90°E centered at about 10°S. The remarkable upwelling in the equatorial region is mostly a result of the meridional overturning equatorial roll, which has northward (southward) surface flow and southward (northward) counterflow underneath with upwelling and downwelling on each side, during the summer (winter) monsoon season. Thus, this upwelling is accompanied by downwelling of similar magnitude (Fig. 9b), resulting in a near-zero annual mean. However, it does assist the particles in crossing the equator as it connects the Ekman transport of the same direction on both sides of the equator (Schott et al. 2002). The upwelling along the coast of Somalia is also associated with a subduction region farther offshore, which is induced by the summer Findlater (1971) jet. Schott et al. (2002) show that the upwelled water along the Somali coast loses its thermocline water characteristics while recirculating in the two-gyre system and experiencing upwelling and subduction. What happens to the particles in the model is that they recirculate in the two-gyre system while experiencing upwelling along the coast and subduction and offshore and, once they are close enough to the equator, they are transported southward across the equator by the equatorial roll, which occupies the latitude band 3°–4° on both sides of the equator.

The open ocean upwelling in the model is located 2° of latitude south of where the observations suggest (Schott et al. 2002). However, the latitude of the upwelling in the model is consistent with that of the upwelling-related thermocline dooming, which is about 2°–3° south of its counterpart in Levitus climatology (Fig. 6). The seasonality of the upwellings is noticeable (Fig. 10): the coastal upwelling occurs mainly during summer (May–August), while the open ocean upwelling is year-round.

The trajectories of upwelled particles in the surface south of the equator are southwestward (Fig. 8a), consistent with the directions of the Ekman transport (southwestward) and the geostrophic flow (westward) during the summer monsoon. Most of the particles in the sur-

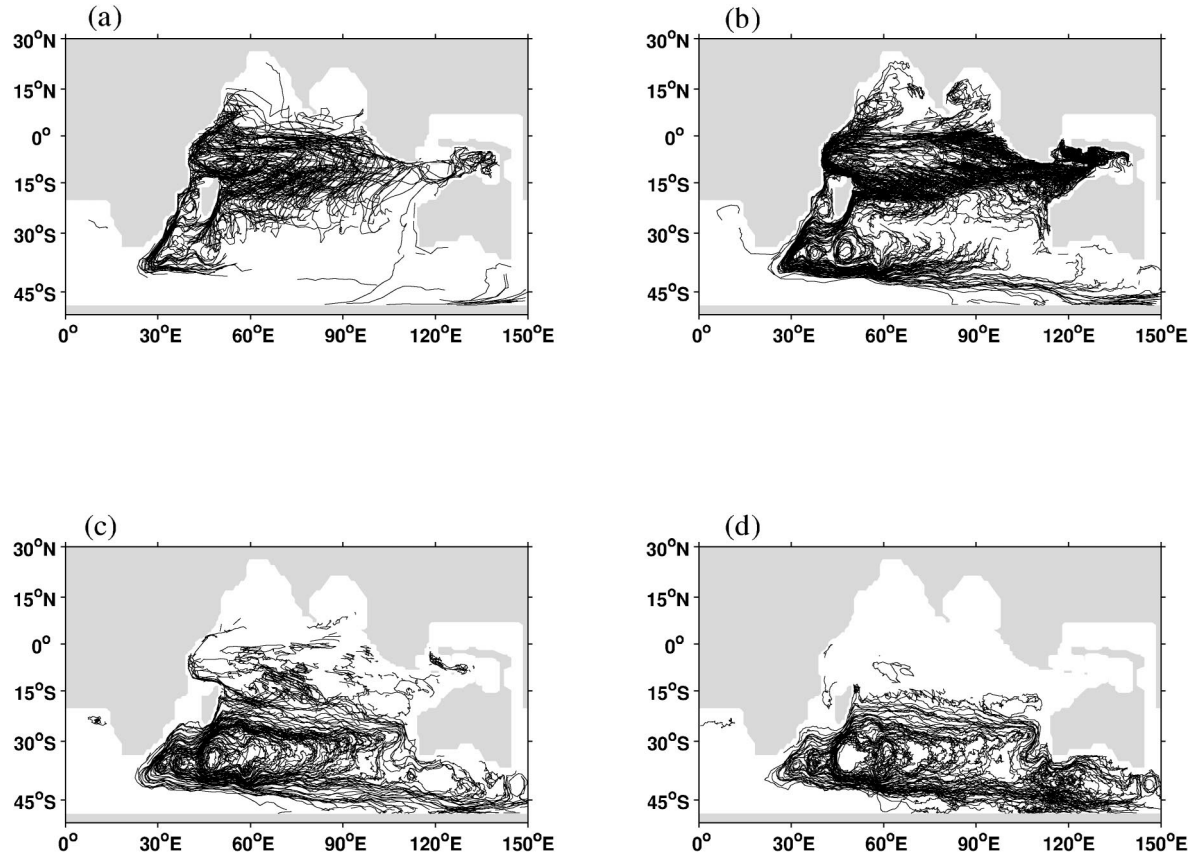

FIG. 8. All particle trajectories of 1 of the 12 Lagrangian trajectory experiments in four vertical layers: (a) <50, (b) 50–200, (c) 200–500, and (d) >500 m.

face layer are not advected to the southern boundary directly. Instead after crossing the SEC they are subducted in the southern subtropics and subsequently transported northward in the upper thermocline to join the SEC. They, then, flow to the western boundary within the SEC and may turn to the south there.

The same experiment procedure is repeated by releasing particles in other density layers slightly different from $\sigma_0 = 24.0$ and 26.0 to test the sensitivity of the pathway described above to where the particles are initially released. It is observed that in those experiments the particle pathways in various layers and the upwelling pattern displayed by the vertical movement of particles are remarkably similar to those shown in Figs. 8 and 9, although the numbers of upwelling and downwelling counted in $2° \times 2°$ bins are slightly different from those in Fig. 9. This is not surprising, given that those upwelling regimes are basically wind driven and they can be manifested by particle trajectories as long as the particles are in the upper thermocline.

The trajectory experiment suggests the importance of upwelling and Ekman transport as a pathway for the ITF water north of the SEC to escape the Indian Ocean. Undoubtably, more observations are needed to further verify the operation of this pathway. However, we gain some confidence from the numerical experiment about the hypothesis that we made based on observations.

The percentages of particles that ever reach certain latitudes north of 8°S are shown in Fig. 11. As compared with the results of Haines et al. (1999), the numbers for 8°S, equator, and 10°N are larger in this study, which possibly results from the fact that we do not restrict particles in the thermocline as they do. The three-dimensional Lagrangian trajectory experiment is summarized in Fig. 12.

6. Transit-time PDF tracer experiment

a. The transit-time PDF

Passive tracers are useful in estimating water ages in the ocean. Naturally the age of a fluid parcel is interpreted as the transit time since the parcel had last contact with the source. However, the fluid particles constituting a fluid parcel are transported to that location through a variety of pathways by advection and diffusion and, hence, have a variety of ages. Strictly speaking, the age of a fluid parcel is not a single quantity but a statistical distribution of transit times of all the fluid particles that constitute the parcel. The concept of transit-time PDF

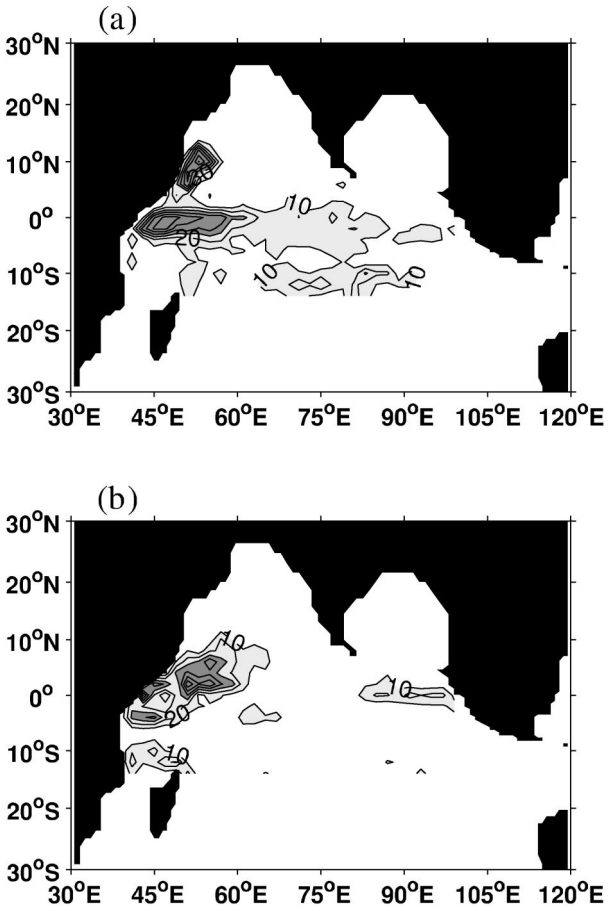

FIG. 9. (a) Contours of the numbers of vertical transfer of particles (sum of all the 12 experiments) upward across the 50-m level in the region between 15°S and 29°N and between 30° and 100°E. The numbers are counted in 2° × 2° bins. The contour interval is 10. The light shaded region has values between 10 and 30, and the dark shaded region is greater than 30. (b) As in (a) but for the vertical transfer downward across the 50-m level.

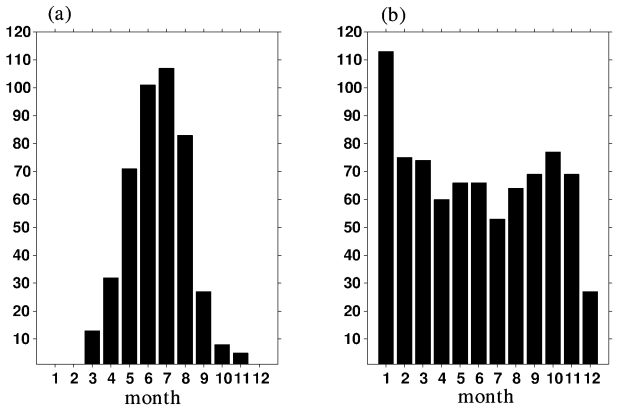

FIG. 10. The seasonal distribution of the numbers of vertical transfer of particles (sum of all 12 experiments) upward across the 50-m level in the two upwelling regions: (a) coastal upwelling between 5° and 12°N and between 40° and 60°E and (b) open-ocean upwelling between 5° and 15°S and between 60° and 90°E.

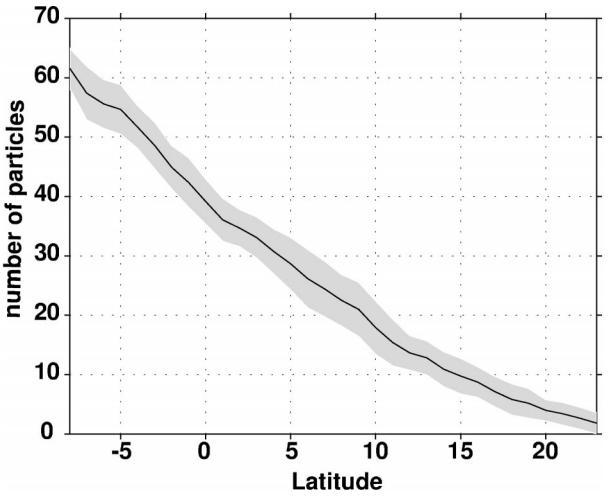

FIG. 11. Percentages of particles that ever reach certain latitudes. Shading indicates the standard deviation.

describes the probability that a fluid parcel has been in the flow for a certain amount of time since last contact with the source region. A brief theoretical derivation of the transit-time PDF can be found in Khatiwala et al. (2001). Suppose the transit-time PDF is $P(\mathbf{X}, t \mid \Omega)$ where $\mathbf{X}$, t, and Ω are the location of the parcel, the elapsed time, and the source region, respectively. In essence, $P(\mathbf{X}, t \mid \Omega)dt$ can be interpreted as the probability that a fluid parcel at $\mathbf{X}$ had last contact with Ω at time between t and $t + dt$ ago. From another perspective, it also represents the volume fraction of a fluid parcel at $\mathbf{X}$ that had last contact with Ω at time between t and $t + dt$ ago.

To practically obtain the PDF of ITF-to-$\mathbf{X}$ transit times in the model, a tracer is released in the source region of the ITF—Makassar Strait—between 100 and 400 m. Tracer values in the source region are set to 1 in the first year and then to 0 afterward. In addition, zero-flux boundary condition is applied to the tracer anywhere else on the boundaries. It should be emphasized that the tracer used here is not dye but the transit-time PDF subjected to peculiar boundary conditions as mentioned above. The model is integrated for 31 years.

b. *Throughflow spreading time scales*

The transit-time PDFs at five different locations are shown in Fig. 13. By definition, the time integral of PDF until infinity is 1. A combination of advection and diffusion is responsible for the shape of PDFs. Generally, the faster the advection is, the earlier is the arrival of the peak, and the stronger the diffusion is, the longer the tail of PDF and the smaller the maximum of PDF are. In this study we refer to the mode of PDF—the elapsed time corresponding to the maximum of PDF—as the most likely age (MLA), which can be interpreted as the advective time scale. In Fig. 13, the fact that the MLA increases and the maximum of PDF decreases

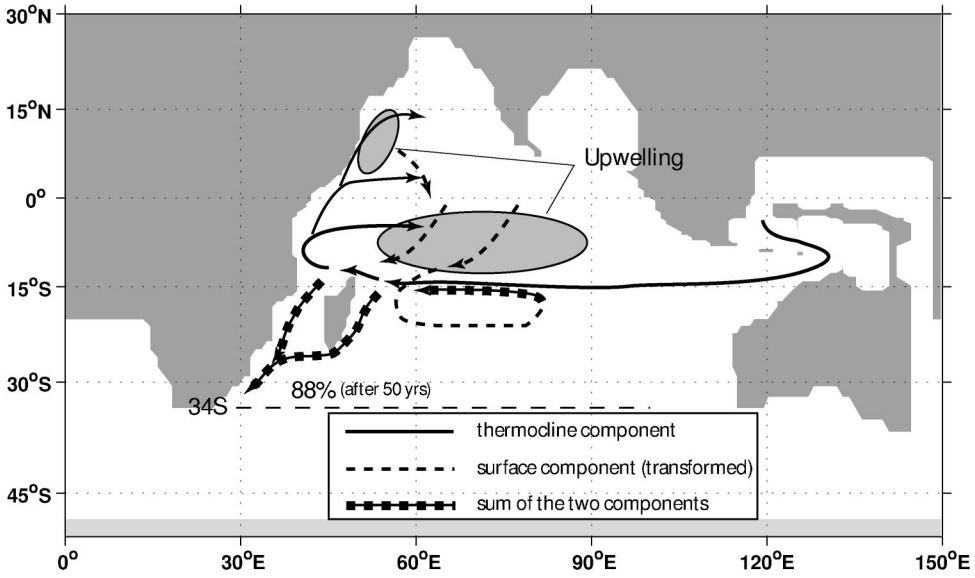

FIG. 12. Summary of the ITF-water-spreading pathways in the three-dimensional Lagrangian trajectory experiment. Note that the pathways have two components: the thermocline component and the surface component that is transformed during upwelling.

with depth (Fig. 13) is a manifestation of slower advection and weaker dominance of the advection over diffusion with depth. The wider peaks and longer tails at locations B and D apparently result from the mixing due to the reversals of the Somali Current and the equatorial currents. By contrast, the dominance of horizontal advection in the SEC results in narrow peaks at locations A and C.

Since the ITF water mostly flows in the upper thermocline, the distributions of MLAs averaged between 100 and 250 m are shown in Fig. 14. The SEC and Leeuwin Current region have the fastest response to the ITF. In this depth range the ITF water crosses the Indian Ocean on a time scale of 10 yr from the Makassar Strait to the east coast of Africa. Haines et al. (1999) show that it takes about 6 years fro the ITF water from 119°E to the western boundary, which is consistent with the corresponding MLAs (6–7 years) shown in Fig. 14. ITF water returns to the east both north and south of the SEC. It takes another 8 years for the ITF water to be advected to the west coast of Australia from the western boundary in the southern subtropics. The ITF water reaches the Arabian Sea over 20 years from the Makassar Strait, which is consistent with the results of Haines et al. (1999) that show that the ITF water reaches 10°N on an average of 18 years from 119°E. The northern Arabian Sea and the Bay of Bengal are the most slowly replenished regions by ITF water in the northern Indian Ocean. MLAs represent the time scales over which the water from the Makassar Strait reaches one location by direct advection. However, because of the complex monsoon circulation in the Indian Ocean, direct advection may not be the main pathway for the ITF water to be transported to various regions in the Indian Ocean. Mixing and diffusion can be important. As shown in Fig. 15, the integrals of PDFs over the 31 years in most regions are still small ($\ll 1$), which means that the majority of a water parcel in those regions had last contact with the source region in the Makassar Strait more than 31 years ago and suggests the dominance of mixing and diffusion in those regions. Since mixing and diffusion tend to destroy the temperature and salinity properties of water masses, we suggest that the MLAs are more appropriate for the spreading time scales of ITF water in the thermocline as a water mass with characteristic temperature and salinity properties.

7. Discussion

a. Uncertainties and limitations

It has to be acknowledged that the numerical experiments have shortcomings, which may affect the results we presented above. The model is forced by monthly mean climatological wind stress, and the lack of variabilities on other frequencies may weaken the representativeness of the Lagrangian trajectories. However, given that seasonal variability, which is the dominant variability in the tropical Indian Ocean, is included in the monthly wind stress climatology, it is not unreasonable to regard the trajectories presented in this paper as a plausible estimate. Furthermore, although introducing more variability in the forcing may modify the quantitative results in section 5, the qualitative feature of the pathway of ITF water north of SEC—upwelling and southward advection in the surface layer—which is one of the main results of this paper, should remain

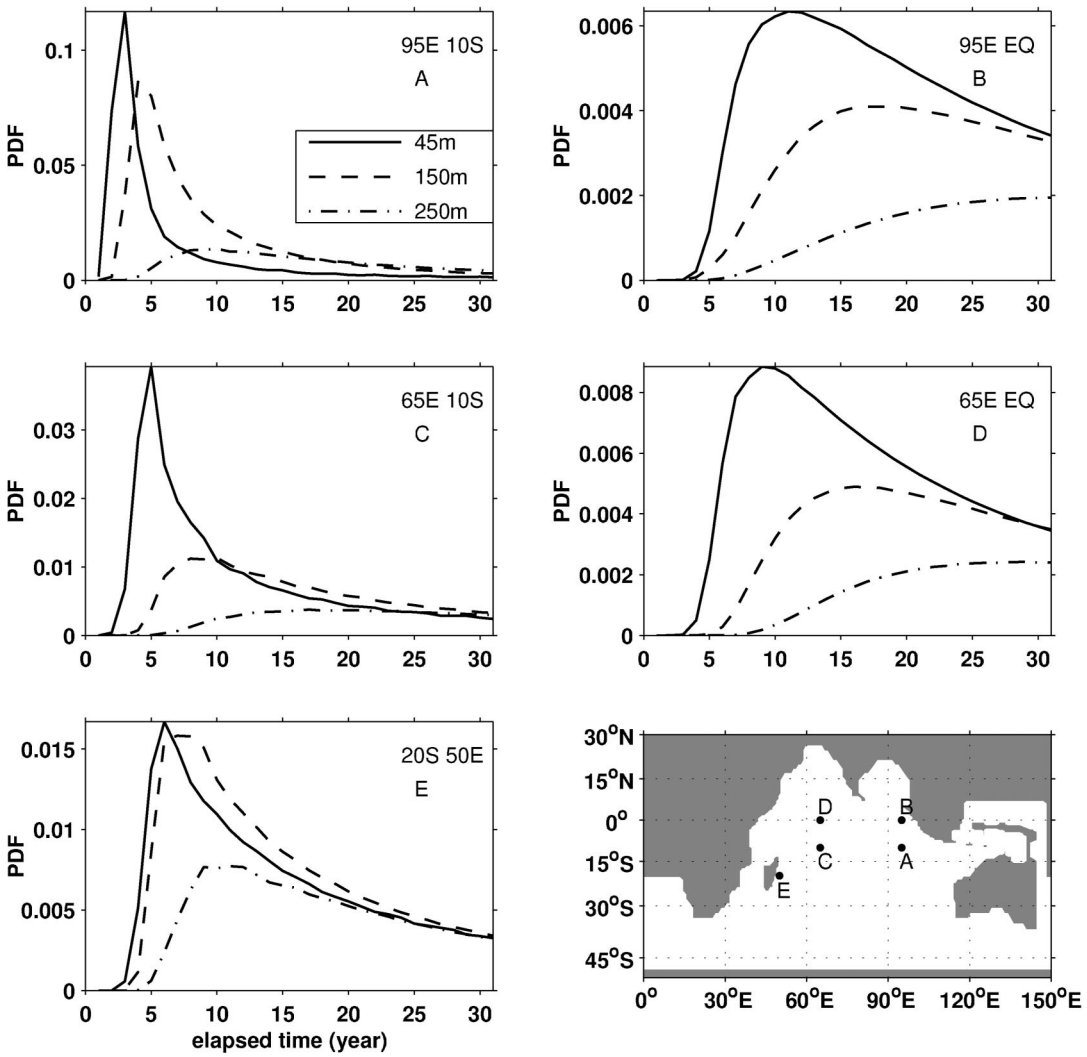

FIG. 13. The transit-time PDF at five different locations for three depth levels (45, 150, and 250 m). The locations are shown in the lower-right panel, and their latitudes and longitudes are indicated in the upper-right corner of each panel.

valid. A similar model study forced by wind stresses with richer variability could be done in the future.

As shown in section 4, the model current speeds in the interior of the basin agree with available ship drift, drifter, and Levitus climatologies but boundary current speeds, particularly the western boundary currents, are underestimated. Therefore, it is reasonable to take the time scale of 10 yr for the ITF water to cross the Indian Ocean within the SEC as a climatological mean value, while the time scales after the ITF reaches the western boundary may be overestimated. But even with 2 more realistic Somali Current, we speculate that the MLAs in the Arabian Sea would still be over 20 years because of the seasonal reversal of the Somali Current.

b. Open-ocean upwelling

The importance of the open-ocean upwelling within the SEG has recently been discussed in several papers. Gartenicht and Schott (1997), Schott and McCreary (2001), and Schott et al. (2002) suggest that the open-ocean upwelling may be an important branch of the shallow meridional overturning circulation. From a dynamic perspective, Xie et al. (2002) conclude that the doming of the thermocline associated with the upwelling enables the subsurface Rossby waves to interact with the atmosphere. Based on the potential importance of upwelling in the diapycnal transfer of ITF water, the upwelling may also allow the ITF to influence the regional air–sea exchange. An interesting question to consider is, does the ITF lead to warmer or cooler upwelling? Less or more ocean heat gain? Assuming that the ITF deepens the thermocline of the Indian Ocean, Godfrey (1996) suspects that, with the ITF opened, the temperature of the upwelled water in the open-ocean upwelling region is increased and hence ocean heat gain in this region is reduced in comparison with a blocked ITF condition. Gordon et al. (1999) observations indi-

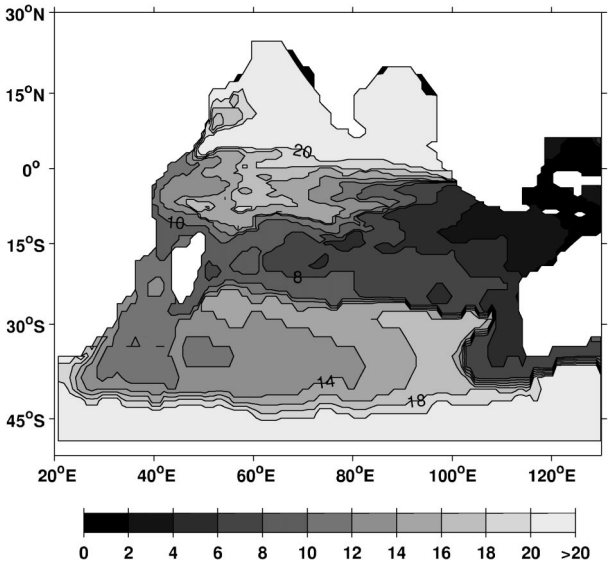

FIG. 14. Distribution of the most likely age averaged between 100 and 250 m.

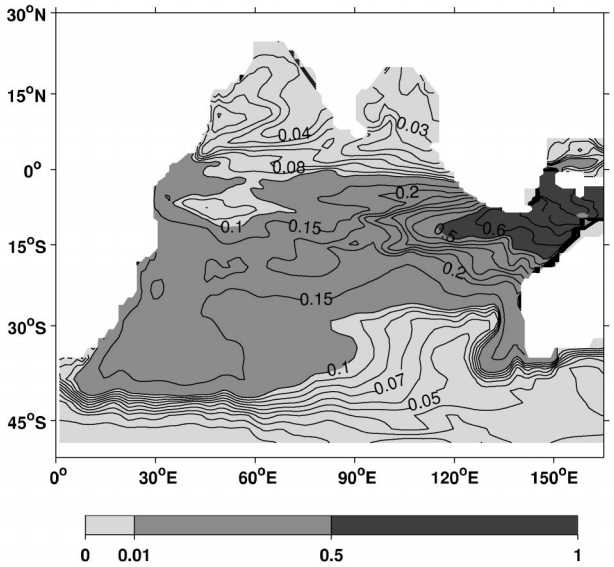

FIG. 15. The integral of the averaged PDFs (between 100 and 250 m) over the 31-yr experiment. Contour intervals are 0.01, 0.05, and 0.1 for the ranges [0–0.1], [0.1–0.5], and [0.5–1], respectively.

cate the ITF is concentrated within the thermocline. Vranes et al. (2002) find that the transport-weighted temperature of the ITF is about 15°C, cooler than the temperature of the tropical Indian Ocean thermocline and much cooler than other authors have suggested. Therefore the net effects of the ITF on the temperature of upwelled water depend on which one of the two competing factors dominates. Further investigation needs to be done on the relative importance of these two factors.

8. Summary

The spreading pathways and time scales of the Indonesian Throughflow in the Indian Ocean are investigated from hydrographic observations and two numerical tracer experiments in an ocean general circulation model, the Lamont Ocean–AML Model. South of the South Equatorial Current, the ITF water within the thermocline is advected to the south through the Mozambique Channel and along the east coast of Madagascar. The pathways of the ITF water that turn northward upon reaching the African coast vary significantly with season. In winter, the ITF water that initially flows northward along the African coast is returned to the interior within the South Equatorial Countercurrent between 3° and 5°S. In summer, the ITF water continues to flow northward along the African margin, cross the equator within the Somali Current, and penetrate farther into the Arabian Sea. The spreading patterns of ITF water are consistent with those from the water mass studies of You and Tomczak (1993) and You (1997).

The tracer experiments support the observational results. Furthermore, the three-dimensional Lagrangian trajectory experiment quantifies the ITF water bifurcation at the western boundary as 38%±5% flowing to the south both through the Mozambique Channel and along the east coast of Madagascar and 62%±5% flowing to the north within the East African Coast Current. These numbers may depend on model configuration (e.g., model resolution) and wind forcing variabilities on other frequencies (recall that monthly wind stress climatology is used in this study). North of the SEC, ITF water is mainly confined in the equatorial region (10°S–10°N), well mixed by the reversal of the equatorial currents, while some penetrates into the Arabian Sea along the western boundary. Only about 20% of ITF water ever reaches 10°N. In Haines et al. (1999) about 11% of particles ever reach 10°N, which may be because they confine their particles in the thermocline layer of their model.

The three-dimensional Lagrangian trajectory experiment also supports the hypothesis based on observations that the main pathway for the thermocline ITF water flowing to the north of SEC to escape the Indian Ocean is through upwelling into the surface layer and the concomitant southward Ekman transport. The upwelling regimes consist of the summer coastal upwelling off Somalia and the year-round open ocean upwelling within the cyclonic ''South Equatorial Gyre,'' roughly between 50° and 90°E and between 5° and 10°S as indicated by Ekman divergence calculations. The latitude of the open ocean upwelling in the model is a couple of degrees south of that shown by observations, but it is consistent with the latitude of thermocline uplift in the model. During upwelling the ITF water in the thermocline loses its characteristic temperature and salinity properties. The equatorial roll, mostly significant in the western equatorial region, plays a role in transporting the transformed ITF water across the equator southward.

The southwestward Ekman transport during the southwest monsoon leads most transformed ITF water in the surface layer to the subtropical convergence zone where it is subducted and transported northward in the thermocline to join the SEC, within which it is advected to the western boundary where it may turn to the south. Therefore, the ultimate passage for the ITF water, either the thermocline ITF water with its defining temperature and salinity properties or the transformed ITF water after upwelling north of SEC, to escape the Indian Ocean is along the western boundary through the Mozambique Channel and along the east coast of Madagascar and subsequently the Agulhas Current region.

This pathway through upwelling engages the ITF water directly into the low-latitude Indian Ocean air–sea heat flux. The specific contribution of the ITF to the magnitude of the air–sea heat flux has been investigated within models with conflicting results (e.g., Hirst and Godfrey 1993; Schneider 1998; Wajsowicz and Schneider 2001). To properly study this topic requires a model that not only contains the correct transport and temperature profile for the ITF, but also properly simulates the seasonal and interannual variability of the ITF and the pathways of ITF water within the Indian Ocean. This study helps to understand the key factors in determining how the ITF affects the air–sea heat flux in the Indian Ocean.

In the transit-time probability density function (PDF) experiment the ITF water spreading time scales are characterized by the *most likely age*, which is the elapsed time corresponding to the maximum of PDF and can be interpreted as the advective time scales. In the upper thermocline the ITF water crosses the Indian Ocean on a time scale of 10 yr and reaches the Arabian Sea on a time scale of over 20 yr. Those results are consistent with the time scales obtained by Haines et al. (1999).

Acknowledgments. The authors thank Naomi Naik, Phil Mele, and Bruce Huber for technical support and advice. Many thanks are given to Dr. Mark Cane and Dr. R. Dwi Susanto for useful comments. We acknowledge the support of National Science Foundation Grant OCE 00-99152.

REFERENCES

Beining, P., and W. Roether, 1996: Temporal evolution of CFC 11 and CFC 12 in the ocean interior. *J. Geophys. Res.*, **101,** 16 455–16 464.

Bolin, B., and H. Rodhe, 1973: A note on the concepts of age distribution and transit time in natural reservoirs. *Tellus*, **25,** 58–62.

Cutler, A. N., and J. C. Swallow, 1984: Surface currents of the Indian Ocean (to 25°S, 100°E): Complied from archived historical data. U.K. Meteorological Office Rep. 187, 42 pp.

de Ruijter, W. P. M., H. Ridderinkhof, J. R. E. Lutjeharms, M. W. Schouten, and C. Veth, 2002: Observations of the flow in the Mozambique Channel. *Geophys. Res. Lett.*, **29,** 1502, 10.1029/2001GL013714.

DiMarco, S. F., P. Chapman, W. D. Nowlin Jr., P. Hacker, K. Donohne, M. Luther, G. C. Hojnson, and J. Toole, 2002: Volume transport and property distribution of the Mozambique Channel. *Deep-Sea Res.*, **49B,** 1481–1511.

Donguy, J., and B. Piton, 1991: The Mozambique Channel revisited. *Oceanol. Acta*, **14,** 549–558.

Fieux, M., C. Andrie, E. Charriaud, A. G. Ilahude, N. Metzl, R. Molcard, and J. C. Swallow, 1996: Hydrological and chlorofluoromethane measurements of the Indonesian throughflow entering the Indian Ocean. *J. Geophys. Res.*, **101,** 12 433–12 454.

Findlater, J., 1971: Mean monthly airflow at low levels over the western Indian Ocean. *Geophys. Mem.*, **16,** 1–53.

Fine, R. A., 1985: Direct evidence using tritium data for throughflow from the Pacific into the Indian Ocean. *Nature*, **315,** 478–480.

Fu, L., 1986: Mass, heat and freshwater fluxes in the south Indian Ocean. *J. Phys. Oceanogr.*, **16,** 1683–1693.

Ganachaud, A., C. Wunsch, J. Marotzke, and J. Toole, 2000: Meridional overturning and large-scale circulation of the Indian Ocean. *J. Geophys. Res.*, **105,** 26 117–26 134.

Garternicht, U., and F. Schott, 1997: Heat fluxes of the Indian Ocean from a global eddy-resolving model. *J. Geophys. Res.*, **102,** 21 147–21 159.

Gent, P., and M. A. Cane, 1989: A reduced gravity, primitive equation model of the upper equatorial ocean. *J. Comput. Phys.*, **81,** 444–480.

——, and J. McWilliams, 1990: Isopycnal mixing in ocean circulation models. *J. Phys. Oceanogr.*, **20,** 150–155.

——, J. Willebrand, T. McDougall, and J. McWilliams, 1995: Parameterizing eddy-induced tracer transports in ocean circulation models. *J. Phys. Oceanogr.*, **25,** 463–474.

Godfrey, J. S., 1996: The effect of the Indonesian throughflow on ocean circulation and heat exchange with the atmosphere: A review. *J. Geophys. Res.*, **101,** 12 217–12 238.

Gordon, A. L., 1986: Interocean exchange of thermocline water. *J. Geophys. Res.*, **91,** 5037–5047.

——, 2001: Interocean exchange. *Ocean Circulation and Climate*, G. Siedler et al., Eds., Academic Press, 303–314.

——, S. Ma, D. B. Olson, P. Hacker, A. Ffield, L. D. Talley, D. Wilson, and M. Baringer, 1997: Advection and diffusion of Indonesian throughflow water within the Indian Ocean South Equatorial Current. *Geophys. Res. Lett.*, **24,** 2573–2576.

——, R. D. Susanto, and A. Ffield, 1999: Throughflow within Makassar Strait. *Geophys. Res. Lett.*, **26,** 3325–3328.

Griffies, S., 1998: The Gent–McWilliams skew flux. *J. Phys. Oceanogr.*, **28,** 831–841.

Gründlingh, M., 1985: Features of the circulation in the Mozambique Basin in 1981. *J. Mar. Res.*, **43,** 779–792.

——, 1993: On the winter flow in the southern Mozambique Channel. *Deep-Sea Res.*, **40B,** 409–418.

Haines, M. A., R. A. Fine, M. E. Luther, and Z. Ji, 1999: Particle trajectories in an Indian Ocean model and sensitivity to seasonal forcing. *J. Phys. Oceanogr.*, **29,** 584–598.

Hall, T. M., and R. A. Plumb, 1994: Age as a diagnostic of stratospheric transport. *J. Geophys. Res.*, **99,** 1059–1070.

Han, W., J. P. McCreary, D. L. T. Anderson, and A. J. Mariano, 1999: Dynamics of the eastern surface jets in the equatorial Indian Ocean. *J. Phys. Oceanogr.*, **29,** 2191–2209.

Harris, T. F. W., 1972: Sources of the Agulhas Current in the spring of 1964. *Deep-Sea Res.*, **19,** 633–650.

Hirst, A. C., and J. S. Godfrey, 1993: The role of Indonesian throughflow in a global ocean GCM. *J. Phys. Oceanogr.*, **23,** 1057–1086.

Holloway, P. E., 1995: Leeuwin current observations on the Australian northwest shelf, May–June 1993. *Deep-Sea Res.*, **42A,** 285–305.

Holzer, M., and T. M. Hall, 2000: Transit-time and tracer-age distributions in geophysical flows. *J. Atmos. Sci.*, **57,** 3539–3558.

Kara, A. B., P. A. Rochford, and H. E. Hurlburt, 2002: Naval Research Laboratory mixed layer depth (NMLD) climatologies. NRL Rep.

NRL/FR/7330-02-9995, 26 pp. [Available from Naval Research Laboratory, Stennis Space Center, MS 39529.]
Khatiwala, S., M. Visbeck, and P. Schlosser, 2001: Age tracers in an ocean GCM. *Deep-Sea Res.*, **48A,** 1423–1441.
Kida, H., 1983: General circulation of air parcels and transport characteristics derived from a hemispheric GCM, Part 2, Very long-term motions of air parcels in the troposphere and stratosphere. *J. Meteor. Soc. Japan,* **61,** 510–522.
Lee, T., I. Fukumori, D. Menemenlis, Z. Xing, and L. Fu, 2002: Effects of the Indonesian Throughflow on the Pacific and Indian Ocean. *J. Phys. Oceanogr.,* **32,** 1404–1429.
Levitus, S., 1988: Ekman volume fluxes for the World Ocean and individual ocean basins. *J. Phys. Oceanogr.,* **18,** 271–279.
——, 1994: World Ocean Atlas 1994: CD-ROM data set documentation. NODC Informal Rep. 13, 30 pp.
Lukas, R., T. Yamagata, and J. McCreary, 1996: Pacific low-latitude western boundary currents and the Indonesian Throughflow. *J. Geophys. Res.,* **101,** 12 209–12 216.
Macdonald, A., 1998: The global ocean circulation: A hydrographic estimate and regional analysis. *Progress in Oceanography,* Vol. 41, Pergamon, 281–382.
——, and C. Wunsch, 1996: A global estimate of the ocean circulation and heat fluxes. *Nature,* **382,** 436–439.
McCreary, J. P., P. K. Kundu, and R. L. Molinari, 1993: A numerical investigation of dynamics, thermodynamics and mixed-layer processes in the Indian Ocean. *Progress in Oceanography,* Vol. 31, Pergamon, 181–244.
Molinari, R. L., D. Olson, and G. Reverdin, 1990: Surface current distributions in the tropical Indian Ocean derived from compilations of surface buoy trajectories. *J. Geophys. Res.,* **95,** 5219–5231.
Murtugudde, R., and A. J. Busalacchi, 1999: Interannual variability of the dynamics and thermodynamics of the tropical Indian Ocean. *J. Climate,* **12,** 2300–2326.
——, ——, and J. Beauchamp, 1998: Seasonal-to-interannual effects of the Indonesian throughflow on the tropical Indo-Pacific Basin. *J. Geophys. Res.,* **103,** 21 425–21 441.
——, S. Signorini, J. Christian, A. Busalacchi, C. McClain, and J. Picaut, 1999: Ocean color variability of the tropical Indo-Pacific basin observed by SeaWiFS during 1997–1998. *J. Geophys. Res.,* **104,** 18 351–18 366.
Nir, A., and S. Lewis, 1975: On tracer theory in geophysical systems in the steady and non-steady state. *Tellus,* **27,** 372–383.
Olson, D. B., G. L. Hitchcock, R. A. Fine, and B. A. Warren, 1993: Maintenance of the low-oxygen layer in the central Arabian Sea. *Deep-Sea Res.,* **40B,** 673–685.
Pacanowski, R., and S. Philander, 1981: Parameterization of vertical mixing in numerical models of the tropical oceans. *J. Phys. Oceanogr.,* **11,** 1443–1531.
Potemra, J. T., R. Lukas, and G. T. Mitchum, 1997: Large-scale estimation of transport from the Pacific to the Indian Ocean. *J. Geophys. Res.,* **102,** 27 795–27 812.
Quadfasel, D., 1982: Low frequency variability of the 20°C isotherm topography in the western equatorial Indian Ocean. *J. Geophys. Res.,* **87,** 1990–1996.
——, and G. R. Cresswell, 1992: A note on the seasonal variability of the south Java Current. *J. Geophys. Res.,* **97,** 3685–3688.
Rao, R. R., M. L. Robert, and F. F. John, 1989: Evolution of the climatological near-surface thermal structure of the tropical Indian Ocean, 1. Description of mean monthly mixed layer depth, and sea surface temperature, surface current, and surface meteorological fields. *J. Geophys. Res.,* **94,** 10 801–10 815.
Richardson, P. L., and T. K. McKee, 1989: Surface velocity in the equatorial oceans (20°N–20°S) calculated from historical ship drifts. Woods Hole Oceanography Institution Tech. Rep. WHOI-89-9, 50 pp.
Ridgway, K. R., J. R. Dunn, and J. L. Wilkin, 2002: Ocean interpolation by four-dimensional weighted least squares—Application to the waters around Australasia. *J. Atmos. Oceanic Technol.,* **19,** 1357–1375.
Sætre, R., and A. J. de Silva, 1984: The circulation of the Mozambique Channel. *Deep-Sea Res.,* **31,** 485–508.
Schiller, A., J. S. Godfrey, P. C. McIntosh, G. Meyers, and S. E. Wijffels, 1998: Seasonal near-surface dynamics and thermodynamics of the Indian Ocean and Indonesian Throughflow in a global ocean general circulation model. *J. Phys. Oceanogr.,* **28,** 2288–2312.
Schneider, N., 1998: The Indonesian Throughflow and the global climate system. *J. Climate,* **11,** 676–689.
Schott, A. F., and J. McCreary, 2001: The monsoon circulation of the Indian Ocean. *Progress in Oceanography,* Vol. 51, Pergamon, 1–123.
——, M. Fieux, J. Kindle, J. Swallow, and R. Zantopp, 1988: The boundary currents east and north of Madagascar. Part II: Direct measurements and model comparisons. *J. Geophys. Res.,* **93,** 4963–4974.
——, J. Reppin, J. Fischer, and D. Quadfasel, 1994: Currents and transports of the Monsoon Current south of Sri Lanka. *J. Geophys. Res.,* **99,** 25 127–25 141.
——, M. Dengler, and R. Schoenefeldt, 2002: The shallow overturning circulation of the Indian Ocean. *Progress in Oceanography,* Vol. 53, Pergamon, 57–103.
Shenoi, S. S. C., P. K. Saji, and A. M. Almeida, 1999: Near-surface circulation and kinetic energy in the tropical Indian Ocean derived from Lagrangian drifters. *J. Mar. Res.,* **57,** 885–907.
Smith, R. L., A. Huyer, J. S. Godfrey, and J. A. Church, 1991: The Leeuwin Current off western Australia, 1986–1987. *J. Phys. Oceanogr.,* **21,** 322–345.
Swallow, J., 1984: Some aspects of the physical oceanography of the Indian Ocean. *Deep-Sea Res.,* **31,** 639–650.
——, R. L. Molinari, J. G. Bruce, O. B. Brown, and R. H. Evans, 1983: Development of near surface flow pattern and water mass distribution in the Somali Basin in response to the southwest monsoon of 1979. *J. Phys. Oceanogr.,* **13,** 1398–1415.
——, M. Fieux, and F. Schott, 1988: The boundary currents east and north of Madagascar, 1. Geostrophic currents and transports. *J. Geophys. Res.,* **93,** 4951–4962.
Tomczak, M., and S. Godfrey, 1994: *Regional Oceanography: An Introduction.* Pergamon, 422 pp.
Trenberth, K., J. Olson, and W. Large, 1989: A global ocean wind stress climatology based on ECMWF analyses. NCAR Tech. Rep. NCAR/YN-338 + STR, 93 pp.
Verschell, M., J. Kindle, and S. Howden, 1995: Effects of Indo-Pacific throughflow on the upper tropical Pacific and Indian Ocean. *J. Geophys. Res.,* **100,** 18 409–18 420.
Vranes, K., A. L. Gordon, and A. Ffield, 2002: The heat transport of the Indonesian throughflow and implications for the Indian Ocean heat budget. *Deep-Sea Res.,* **49B,** 1391–1410.
Wajsowicz, R. C., 2001: Air–sea interaction over the Indian Ocean due to variations in the Indonesian Throughflow. *Climate Dyn.,* **18,** 437–453.
——, and E. K. Schneider, 2001: The Indonesian Throughflow's effect on global climate determined from the COLA Coupled Climate System. *J. Climate,* **14,** 3029–3042.
Warren, B. A., 1981: Trans-Indian hydrographic section at latitude 18°S: Property distributions and circulation in the South Indian Ocean. *Deep-Sea Res.,* **28,** 759–788.
——, H. Stommel, and J. C. Swallow, 1966: Water masses and pattern of flow in the Somali Basin during the southwest monsoon of 1964. *Deep-Sea Res.,* **13,** 825–860.
Webster, P., V. O. Magana, T. N. Palmer, J. Shukla, R. A. Tomas, M. Yanai, and T. Yasunari, 1998: Monsoons: Processes, predictability, and the prospects for prediction. *J. Geophys. Res.,* **103,** 14 451–14 510.
Wijffels, S., J. Sprintall, M. Fieux, and N. Bray, 2002: The JADE and WOCE I10/IR6 throughflow sections in the southeast Indian Ocean. Part 1: Water mass distribution and variability. *Deep-Sea Res.,* **49B,** 1341–1362.
Wyrtki, K., 1971: *Oceanographic Atlas of the International Indian Ocean Expedition.* National Science Foundation, 531 pp.

——, 1973: An equatorial jet in the Indian Ocean. *Science,* **181,** 262–264.

Xie, S., H. Annamalai, F. A. Schott, and J. P. McCreary, 2002: Structure and mechanisms of south Indian Ocean climate variability. *J. Climate,* **15,** 864–878.

You, Y., 1997: Seasonal variations of thermocline circulation and ventilation in the Indian Ocean. *J. Geophys. Res.,* **102,** 10 391–10 422.

——, and M. Tomczak, 1993: Thermocline circulation and ventilation in the Indian Ocean derived from water mass analysis. *Deep-Sea Res.,* **40A,** 13–56.